Forecasting of Tropospheric Delay Using AI Foundation Models in Support of Microwave Remote Sensing

Junsheng Ding, Xiaolong Mi, Wu Chen, Junping Chen, *Member, IEEE*, Jungang Wang, Yize Zhang, Joseph L. Awange, Benedikt Soja, *Member, IEEE*, Lei Bai, Yuanfan Deng, and Wenjie Tang

***Abstract*— Accurate tropospheric delay forecasts are imperative for microwave-based remote sensing techniques, playing a pivotal role in early warning and forecasting of natural disasters such as tsunamis, heavy rains, and hurricanes. Nevertheless, conventional methods for forecasting tropospheric delays entail substantial computational resources and high network transmission speeds, thereby restricting their real-time applicability in remote sensing operations. In this study, we introduce a novel approach to derive forecasted tropospheric delays using artificial intelligence (AI) weather forecast foundation models (FMs), exemplified by Huawei Cloud Pangu-Weather, Google DeepMind GraphCast, and Shanghai AI Lab FengWu. We assess the accuracy of these forecasts on a global scale employing fifth-generation ECMWF atmospheric re-analysis of the global climate (ERA5) (European Centre for Medium-Range Weather Forecasts (ECMWF) Reanalysis v5), ground-based Global Navigation Satellite System (GNSS), and in situ radiosonde (RS) measurements as reference data. Our results show that the FM-based scheme outperforms traditional methods in both forecast accuracy and length, with the ability to provide high-accuracy tropospheric delay parameters locally for 15-day forecasts at any location within minutes. Furthermore, the FM scheme still maintains accuracy better than empirical models when forecasting up to ten days in advance. This research demonstrates the potential of AI weather forecast FMs in delivering high-precision tropospheric delay medium-range forecasts and improvements for real-time remote sensing applications.**

***Index Terms*— Artificial intelligence (AI), foundation models (FMs), global model of pressure and temperature 3 (GPT3), high accuracy, Vienna mapping functions 3 forecast version (VMF3_FC).**

NOMENCLATURE

3DEST	3-D Earth-specific transformer.
4D-Var	4-D variational data assimilation.
ACC	Anomaly correlation coefficient.
AI	Artificial intelligence.
BIAS	Mean of bias.
ECMWF	European Centre for Medium-Range Weather Forecasts.
ERA5	Fifth-generation ECMWF atmospheric re-analysis of the global climate.
FLOPS	Floating-point operations per second.
FM	Foundation models.
Ge	East gradient.
Geh	Hydrostatic east gradient.
Gew	Wet east gradient.
Gn	North gradient.
Gnh	Hydrostatic north gradient.
GNN	Graph neural network.
GNSS	Global Navigation Satellite System.
Gnw	Wet north gradient.
GPT3	Global model of pressure and temperature 3.
HRES	High-resolution forecasting.
IFS	Integrated forecasting system.
IGRA	Integrated Global Radiosonde Archive.
InSAR	Interferometric synthetic aperture radar.
MSLP	Mean sea-level pressure.
NCAR	National Center for Atmospheric Research.
NGL	Nevada Geodetic Laboratory.
NOAA	National Oceanic and Atmospheric Administration.
NWM	Numerical weather model.
NWP	Numerical weather prediction.
RMSE	Root-mean-square error.

Received 3 March 2024; revised 9 October 2024; accepted 28 October 2024. Date of publication 1 November 2024; date of current version 21 November 2024. This work was supported in part by the General Research Fund of Hong Kong under Grant 15229622, in part by the Innovation and Technology Fund of Hong Kong under Grant ITP/019/22LP, in part by the National Natural Science Foundation of China under Grant 11673050 and Grant 42474034, in part by the Key Program of Special Development Funds of Zhangjiang National Innovation Demonstration Zone under Grant ZJ2018-ZD-009, in part by the National Key Research and Development Program of China under Grant 2018YFB0504300, and in part by the Key Research and Development Program of Guangdong Province under Grant 2018B030325001. *(Corresponding author: Junping Chen.)*

Junsheng Ding, Xiaolong Mi, Wu Chen, and Yuanfan Deng are with the Department of Land Surveying and Geo-Informatics, The Hong Kong Polytechnic University, Hong Kong, China (e-mail: junshengding@yeah.net; xiaolong.mi@polyu.edu.hk; wu.chen@polyu.edu.hk; yuanfan.deng@connect.polyu.hk).

Junping Chen, Yize Zhang, and Wenjie Tang are with Shanghai Astronomical Observatory, Chinese Academy of Sciences, Shanghai 200030, China, and also with the School of Astronomy and Space Science, University of Chinese Academy of Sciences, Beijing 100049, China (e-mail: junping@shao.ac.cn; zhyize@shao.ac.cn; tangwj@shao.ac.cn).

Jungang Wang is with the Department of Geodesy, GeoForschungsZentrum (GFZ), 14473 Potsdam, Germany, and also with the Institut für Geodäsie und Geoinformationstechnik, Technische Universität Berlin, 10623 Berlin, Germany (e-mail: jgwang@gfz-potsdam.de).

Joseph L. Awange is with the School of Earth and Planetary Sciences, Curtin University, Perth, WA 6845, Australia (e-mail: J.Awange@curtin.edu.au).

Benedikt Soja is with the Institute of Geodesy and Photogrammetry, ETH Zürich, 8093 Zürich, Switzerland (e-mail: soja@ethz.ch).

Lei Bai is with Shanghai AI Laboratory, Shanghai 200030, China (e-mail: bailei@pjlab.org.cn).

Digital Object Identifier 10.1109/TGRS.2024.3488727

RS	Radiosonde.
SA	Satellite altimetry.
SP	Surface pressure.
T2M	2-m temperature.
TCWV	Total column water vapor.
TP	Total precipitation.
TPUv4	Fifth Google domain-specific architecture and its third supercomputer for such machine learning models.
U10	10-m u wind component.
V10	10-m v wind component.
VLBI	Very long baseline interferometry.
VMF3_FC	Vienna mapping functions 3 forecast version.
ZHD	Zenith hydrostatic delay.
ZTD	Zenith tropospheric delay.
ZWD	Zenith wet delay.

I. Introduction

THE propagation of electromagnetic waves through the neutral atmosphere is subject to delays and bending caused by gas molecules, leading to a measurement error known as tropospheric delay [1], [2]. This delay cannot be mitigated by multifrequency signals due to the nondispersive nature of the neutral atmosphere—unlike the ionosphere—thus necessitating the use of models or observational estimates to correct its effects [3], [4], [5]. Inaccurate tropospheric delay models can lead to distorted remote sensing images [6], misleading crustal deformation signals [7], and biases in navigation and positioning [8] on one hand. Its accurate determination on the other hand can enhance estimation and understanding of the spatial–temporal distribution of water vapor, a greenhouse gas [9], [10], [11], [12], [13]. Therefore, highly accurate tropospheric delay models are essential for microwave-based remote sensing applications.

The accuracy of tropospheric delay models depends on the quality of meteorological data, with NWMs being the primary source for generating high-accuracy tropospheric delay models. For example, the GPT series models are empirical models [14], [15], [16] of tropospheric delay based on the NWM and the series products [16], [17], [18] are discrete tropospheric delay products based on the NWM [19], [20]. Tropospheric delays derived from NWMs are utilized in various Earth observation techniques, including SA [21], [22], InSAR [23], [24], VLBI [25], [26], and GNSSs [27], [28], [29], contributing to improved precision and reliability in these applications [30], [31]. In addition, NWM-derived tropospheric delays play a crucial role in early warning systems for geodynamic disasters such as volcanic eruptions [32] or earthquakes [33], [34], and weather-related disasters such as hurricanes [35] and floods [36].

NWM-derived tropospheric delays play an important role in the postprocessing and real-time Earth observation applications mentioned above [20], [37], especially for real-time applications, e.g., extreme weather monitoring and disaster assessment require forecasted tropospheric delays, which are typically obtained from empirical models or NWP models [18]. Empirical models extract the spatial and temporal patterns of a large amount of historical atmospheric states and then express them as functions and/or grids. Empirical models are very easy to use but usually do not contain detailed information on atmospheric changes on one hand, and the achievable accuracy is limited on the other hand [38], [39]. The generation of NWP is based on computer simulations that require complex calculations using supercomputers, usually provided by large meteorological agencies such as the ECMWFs and the NCAR [40], [41]. Users need to continuously download these NWP data to apply them in real-time settings. This process of acquiring real-time tropospheric delay places significant demands on the user's network transmission speed. The existing tropospheric delay forecast products VMF1_FC and VMF3_FC (forecast version of VMF1 and VMF3), for example, provide data for only four epochs (H00, H06, H12, and H18) per day for the next day and at specific grid points or station sites [16], [18]. Because of these reasons, the broad application of forecast tropospheric delays in real-time remote sensing is restricted.

Recently, the largest and most dominant companies in the information technology (IT) industry, such as Nvidia, Huawei, and Google, have used AI technology to spearhead the development of more efficient weather forecasting FMs [42], [43], [44]. Based on the enormous computational prowess of the tech giants, these AI FMs are trained on decades of global NWM reanalysis data; however, once trained, inference forecasting using these models requires very little computational work. Forecasts from these models have shown the potential to exceed traditional methods by orders of magnitude in efficiency, allowing users to locally generate 15-day or longer forecasts in a short period. These forecasts have been shown to display comparable or better severe events prediction for tropical cyclones, atmospheric rivers, and extreme temperatures [44], [45]. Since the primary goal of these FMs is medium-range weather forecasting, only a small number of NWM meteorological variables are involved in the training of the models. Fortunately, the variables needed to calculate the refractive index to generate tropospheric delays are included in some of the abovementioned FMs. Therefore, this technological revolution presents an opportunity for microwave-based remote sensing techniques to benefit from the use of FMs for tropospheric delay forecasting.

Despite the great potential of the FMs for natural language processing, computer vision, and weather forecasting, to the best of the authors' knowledge, there are no relevant studies on tropospheric delays. In an attempt to fill this gap, this contribution proposes a scheme for obtaining high-accuracy forecasted tropospheric delays based on the FMs and comprehensively evaluates the accuracy of the forecasted tropospheric delay parameters, including zenith delay ZHD and ZWD, mapping function [hydrostatic mapping function coefficient (ah) and wet mapping function coefficient (aw)], tropospheric gradient (Gnh, Geh, Gnw, and Gew), and three meteorological parameters of pressure (P), temperature (T) and water vapor pressure (e). In the experiments, the ERA5, global ground-based GNSS tropospheric delays, and in situ RS observations are used as references, and the results from the existing forecasted tropospheric delay products VMF3_FC as well as

TABLE I
PROPERTIES OF WEATHER FORECAST MODELS

Model (release)	Affiliation (parameters)	Model Type (AI technique)	Variables	Computational Cost	Training Cost
HRES (1997-11-25) [46]	ECMWF	NWM	A series of surface variables at single level and atmospheric variables* at 25 pressure levels	About 1 hour for 72 Nvidia A100 GPUs (312 tera FLOPS).	————
Pangu-Weather (2023-1-5) [43]	Huawei Cloud **(64M)**	FM (3DEST)	4 surface variables (MSLP, U10, V10, T2M) at single level + 5 atmospheric variables (Z, Q, T, U and V at 13 pressure levels	1.4 s on a Tesla-V100 GPU (120 tera FLOPS)	Approximately 16 days on a cluster of 192 Nvidia Tesla-V100 GPUs.
GraphCast (2022-12-24) [44]	Google DeepMind **(36.7M)**	FM (GNN)	5 surface variables (MSLP, U10, V10, T2M, and **TP**) at single level + 6 atmospheric variables (Z, Q, T, U, V and **W** at 13 or **37** pressure levels	60 s on a Google TPUv4 GPU (275 tera FLOPS)	Four weeks on 32 TPUv4 GPUs.
FengWu (2023-4-6) [45]	Shanghai AI Lab	FM (Transformer)	4 surface variables (MSLP, U10, V10, T2M) at single level + 5 atmospheric variables (Z, Q, T, U and V at 13 or **37** pressure levels	0.6 s on a Tesla-A100 GPU (312 tera FLOPS)	17 days on a cluster of 32 Nvidia A100 GPUs.

*HRES variables: https://www.ecmwf.int/en/forecasts/datasets/set-i#I-i-a_fc, see TABLE II for full names of variables.

the results calculated by employing the empirical model GPT3 are included in the comparison and evaluation.

II. DATA AND METHODOLOGY

This section provides an overview of the traditional weather forecasting model and AI weather forecasting FMs used to infer the forecasted Earth's atmospheric states and describes the tropospheric products used for validation and comparison, including discrete and empirical models. In addition, two sources of tropospheric delay used as a reference are discussed.

A. Weather Forecasting Models

The ECMWF's IFS is at the forefront of traditional weather forecasting. As a component of the IFS, ECMWF's HRES is the top deterministic operational system in the world, providing global weather forecasts every 6 h with exceptional accuracy [44], [46]. These models are based on extensive data assimilation and high-performance computing, enabling the generation of ten-day forecasts in hours.

In addition to traditional models, AI-based weather forecasting models have emerged as powerful tools for predicting weather patterns. FourCastNet, developed by Nvidia, is the first deep learning model to predict surface winds globally. While slightly less accurate than IFS, FourCastNet offers significantly faster predictions and energy savings [43], making it a valuable addition to the forecasting landscape.

Pangu-Weather, proposed by Huawei Cloud, is another noteworthy global AI weather forecasting system. Constructed based on 3DEST, Pangu-Weather has surpassed traditional numerical forecasting methods in accuracy and prediction trends for extreme weather events. Its performance in predicting tropical storm paths is particularly notable, showcasing the potential of FM-based models in weather forecasting [43]. Note that the vertical resolution of Pangu-Weather is only 13 layers. The meteorological variables at these pressure levels can be used to calculate the tropospheric delay, but the coarse resolution may lead to accuracy degradation, which is analyzed and discussed in detail in this study.

GraphCast, developed by Google DeepMind, is a state-of-the-art weather forecasting FM based on GNN technology. Its "encode-process-decode" configuration with GNN as the backbone has demonstrated superior performance, outperforming Pangu-Weather on 99.2% of its targets [44]. GraphCast supports ERA5's highest 37 pressure-level atmospheres as inputs, one of the most important to assess in our study.

FengWu, proposed by Shanghai AI Laboratory, is another advanced weather forecast FM. FengWu is built based on multimodal and multitask deep learning methods and performs better than GraphCast in predicting 80% of the 880 reported predictands [45]. FengWu also supports ERA5's highest 37 pressure-level atmospheres, which is an important aspect for the objectives of this study. The affiliation, technology, variables, and cost of traditional weather forecasting model HRES and the FMs used in this study are listed in Table I. The surface variables at the single level and atmospheric variables at the pressure level for each model are shown in Table II.

B. Tropospheric Reference Models

This section provides a brief description of the following three models: ERA5, the NWM used as the input to the FM's

TABLE II
WEATHER VARIABLES AND LEVELS MODELED BY *FourCastNet* ∗, **PANGU**, FENGWU, GRAPHCAST, AND VMF3_FC

Single-level variables (5)	Pressure-level variables (6)	Pressure levels (37) unit: hPa
Mean sea-level pressure (MSLP)	***Geopotential (Z)***	1, 2, 3, 5, 7, 10, 20, 30, ***50***, 70, **100**, 125,
10 m u wind component (U10)	**Specific humidity (Q)**	**150**, 175, **200**, 225, **250**, **300**, 350, **400**,
10 m v wind component (V10)	***Temperature (T)***	450, ***500***, 550, **600**, 650, **700**, 750, 775,
2 m temperature (T2M)	***U component of wind (U)***	800, 825, ***850***, 875, 900, **925**, 950, 975,
Total precipitation (TP)	***V component of wind (V)***	***1000***
Surface pressure (SP)	Vertical wind speed (W)	
	Relative humidity (RH)	

* FourCastNet requires [U, V, Z] at 1000 hPa, [T, U, V, Z, RH] at 850 hPa and 500 hPa, and only [Z] at 50 hPa, in addition to Integrated TCWV (Total Column Water Vapor) for FourCastNet. FengWu have the same variables with Pangu-Weather but its full version supports 37 levels of pressure levels.

initial atmospheric state; VMF3_FC, a discrete tropospheric delay forecast product; and the empirical model GPT3, which is used as a reference to evaluate the FMs' decline in precision with forecast duration. These models were chosen based on their representative accuracy and widespread acceptance within the scientific community.

1) Numerical Weather Model: ERA5 is the fifth-generation ECMWF atmospheric reanalysis of the global climate, providing hundreds of static, surface, and atmospheric variable values for the period from January 1940 to the present at a resolution of 0.25° latitude/longitude in 1-h increments. The dataset is based on reanalysis using ECMWF's HRES model (cycle 42r1) within ECMWF's 4D-Var system [44], [47]. Numerous studies have demonstrated the superior accuracy of the ERA5 dataset in describing the actual atmospheric situation [10], [48], [49]. The AI FMs mentioned in this research are trained based on ERA5 data.

2) Discrete Troposphere Delay Model: VMF3_FC is a forecast tropospheric delay product produced by Technische Universität Wien using forecast ECMWF data [16]. It provides zenith delays, mapping functions, and gradients for different forecast lengths. The model has been shown to adequately predict and capture changing ZHD, significantly improving positioning accuracy and retrieving high-precision precipitable water vapor (PWV) [12], [50], [51], [52], [53], [54]. We used the VMF3_FC forecasts from 2022 as the latest year is only available under a separate license agreement. In this study, 00z, 06z, 12z, and 18z refer to the epochs 00:00, 06:00, 12:00, and 18:00, respectively; these four moments correspond to different forecast lengths. In the VMF series products, they have H00, H06, H12, and H18 as file name suffixes. Table III shows the properties of forecast length of the VMF3_FC products and the forecast steps of different FMs when comparing them with VMF3_FC.

3) Empirical Troposphere Delay Model: GPT3 is an empirical model released by the Technische Universität Wien and based on more than ten years of monthly averaged data from ECMWF [16]. The model has achieved a global-scale ZTD accuracy of 4.41 cm [55] and has been continuously refined in subsequent studies [56], [57], [58], [59]. While these refinements have achieved numerical improvement, the model primarily outputs zenith delays and rarely includes parameters such as gradient and mapping functions. The inclusion of GPT3 results in the comparison allows for the assessment of the accuracy of AI FMs, particularly as the accuracy deteriorates with longer forecasting horizons. This is an important comparison because when the predictive performance is worse than that of the empirical model, it becomes meaningless to continue with the forecast.

TABLE III
PROPERTIES OF THE FORECAST LENGTH OF DIFFERENT FORECAST MODELS

VMF3_FC	00z (H00)	06z (H06)	12z (H12)	18z (H18)
Pangu-Weather	24h	24h+6h	24h+2×6h	24h+3×6h
GraphCast	4 steps×6h	5 steps×6h	6 steps×6h	7 steps×6h
FengWu	4 steps×6h	5 steps×6h	6 steps×6h	7 steps×6h
Forecast length	24h	30h	36h	42h

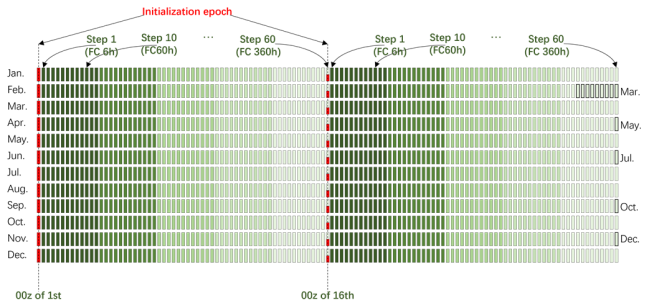

Fig. 1. Graphical representation of 15-day forecast using 2022 data. Each small square represents an epoch; the red square represents the initial epoch, which is obtained from ERA5; and the green square represents the forecast epoch, which is obtained from the forecast.

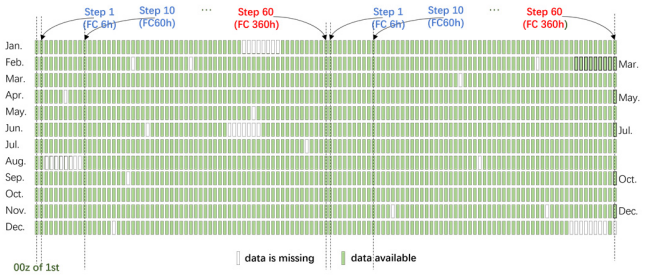

Fig. 2. Graphical representation of selection strategy of active GNSS and RS stations. The graph shows the missing or active data records for a ground-based or in situ measurement. For example, there is available data for all 24 epochs corresponding to steps 1 and 10, and this station participates in the calculation of RMSE for steps 1 and 10, whereas in step 60, there is one missing data point, i.e., the data for the 00z epoch of December 31; then, this station does not participate in the calculation of RMSE for step 60.

TABLE IV
PROPERTIES OF TROPOSPHERIC DELAYS FROM NWMS

Factors	Specification
NWM	ERA5; Pangu-Weather; GraphCast, FengWu
Inference steps	60 steps (15 days); 8 steps (2 days)
Step length	6 hours
Elevation angles	3°
Azimuth angles	8 [0°: 45°: 315°]
Horizontal resolution	1°×1°
Horizontal coverage	lat: [89.5°, −89.5°], lon: [0.5°, 359.5°], 64800 grid points; ~20,000 NGL GNSS sites; ~2,800 IGRA Radiosonde sites
Vertical coverage	13 (Pangu-Weather) and 37 (GraphCast and FengWu) pressure levels
Initial epoch	00z on the 1st and 16th of each month in 2022 for 15-day predictions (total 24×60=1440 epochs); 00z on every day in 2022 for 2-day predictions (total 365×8=2920 epochs)

TABLE V
MEAN BIAS (BIAS) AND RMSE OF TROPOSPHERIC DELAYS DERIVED FROM 13-PRESSURE-LEVEL ERA5 AND 25-PRESSURE-LEVEL ERA5 DATA WITH THOSE DERIVED FROM 37-PRESSURE-LEVEL ERA5 DATA IN 2022 AS A REFERENCE

Parameters	BIAS		RMSE	
	13 levels	25 levels	13 levels	25 levels
ZHD (mm)	-1.10	0.29	10.25	0.53
ZWD (mm)	-3.44	-2.16	5.19	2.89
ah (e-6)	-0.65	-0.08	8.16	0.30
aw (e-5)	-0.49	-0.51	3.87	2.71
Gnh (mm)	-0.016	0.000	0.065	0.013
Gnw (mm)	0.000	0.000	0.064	0.048
Geh (mm)	0.000	0.000	0.029	0.011
Gew (mm)	0.000	0.000	0.056	0.043
P (hPa)	0.029	0.005	0.076	0.048
T (K)	-0.015	0.003	0.396	0.252
e (hPa)	0.177	0.085	0.596	0.378

TABLE VI
MEAN BIAS (BIAS) AND RMSE OF ZTD, GN, AND GE DERIVED FROM 13-, 25-, AND 37-PRESSURE-LEVEL ERA5 DATA WITH TROPOSPHERIC PRODUCTS FROM 338 NGL GNSS STATIONS IN 2022 AS A REFERENCE

Factors	BIAS			RMSE		
	13-level	25-level	37-level	13-level	25-level	37-level
ZTD (mm)	-9.97	-3.75	-1.88	18.66	12.99	10.99
Gn (mm)	-0.099	-0.119	-0.120	0.751	0.768	0.754
Ge (mm)	0.098	0.095	0.095	0.797	0.796	0.792

C. Tropospheric Reference Observations

NWMs combine dozens of types of sensor observation data and are the optimal reflection of the atmospheric state under the minimum error initial field; it is, however, not a "true" reflection [20]. In situ measurements are considered to be the most accurate reflection of atmospheric conditions; hence, it is necessary to use actual measured data as a reference to evaluate the performance of the AI model. The measured data are affected by factors such as weather conditions, sensor failures, and operator errors, so the data quality is uneven and there are varying degrees of missing data. Therefore, we have selected data from over 19 000 GNSS stations from the NGL and over 2800 RS stations from the IGRA to obtain a representative amount of data for our evaluations [60], [61]. It is important to note that the GNSS data from NGL only provide ZTD, Gn, and Ge, where Gn is the north gradient and Ge is the east gradient. The gradients do not differentiate between hydrostatic and wet components. The stations that fulfill the experimental conditions are not the same under different subexperiments. The distribution of the selected stations for each subexperiment is given together with the experimental results in Section III. The graphical representations (Figs. 1 and 2) are provided to help better understand the details of the experimental setup, including the selection of forecast epochs and the selection strategy for the ground-based or in situ measurements.

D. Experimental Setup and Experimental Methodology

This study comprises three distinct experiments. The first experiment aims to investigate the differences in tropospheric delays calculated from an NWM using different pressure-level configurations. Tropospheric delays in this experiment are all computed using ERA5 in 2022 with a temporal resolution of 6 h and a total of 1460 epochs. The second experiment is focused on determining the accuracy of forecasted troposphere delays using AI FMs, computed on a 1° × 1° grid. The experiment involves two inference steps: 60 steps (15 days) and eight steps (two days). The former aims to access the rate of decrease of the FM precision with an increasing forecast length, while the latter assesses the performance in comparison with VMF3_FC. The third experiment parallels the second but is computed at GNSS and RS sites, using the

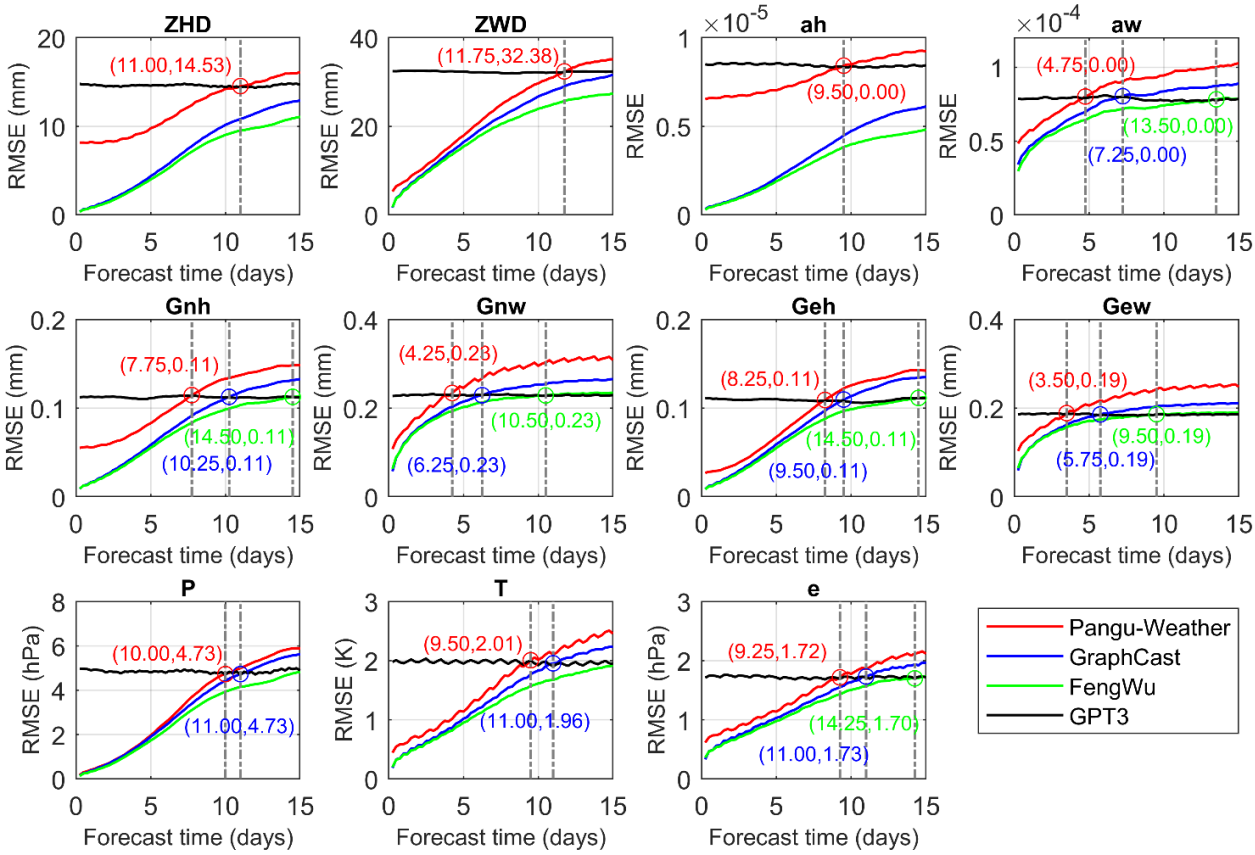

Fig. 3. RMSE of global zenith delays (ZHD and ZWD), mapping function coefficients (ah and aw), gradients (Gnh, Gnw, Geh, and Gew), pressure (P), temperature (T), and water vapor pressure (e) from the Pangu-Weather, GraphCast, and FengWu FMs for 15-day (60 steps, times of 00z, 06z, 12z, and 18z) forecasts and the GPT3 empirical model on 1° × 1° grid. Note that due to the spatial convergence of the grid, the above RMSE is latitude-weighted.

respective measurements as ground truth. The specific details of these experimental setups are provided in Table IV and Figs. 1 and 2.

III. Results and Analyses

In this section, we present the comprehensive results and analyses of our study on tropospheric delays derived from different pressure-level layers and forecast models.

A. Effect of the Number of Pressure Levels on the Experimental Results

GraphCast and Pangu-Weather do not have the same maximum supported output pressure-level layers, and the number of NWM layers used by the VMF3_FC products is also different compared to the former two. Therefore, the impact of the different number of pressure layers on the results needs to be determined first. In this section, tropospheric delays are derived from ERA5 data with 13, 25, and 37 utilized layers (corresponding to Pangu-Weather, VMF3_FC, and GraphCast, respectively). Subsequently, internal and external comparisons are carried out using the results from using 37 pressure levels and the GNSS measurements as a reference.

1) Internal Comparison at Grid Points: The internal comparison was performed on a global 1° × 1° grid using the tropospheric delays derived from 37-level ERA5 as a reference. We calculated the bias and RMSE for the results of the l3- and 25-level configurations. The statistical results in Table V show that the lack of pressure-level layers mainly introduces a negative bias to the tropospheric delay, where the hydrostatic part of the bias was an order of magnitude larger for the 13-level results, compared to using 25 layers. The difference in the wet part was not as significant as in the hydrostatic part, with the bias of the 25-level delays being about one-third smaller than with 13 levels. The RMSE analysis revealed that the ZHD RMSE for 13 levels exceeded 1 cm and was about 20 times higher than the 25-level result. Also, the difference in the mapping function coefficients ah was very large. This suggests that for applications that require precise hydrostatic delays such as high-precision GNSS PWV determination, the Pangu-Weather model may not be suitable. The gradients are not significantly affected by the difference in the number of layers due to their relatively small values. The spatial distributions of bias and RMSE for the 11 tropospheric delay parameters in Table V are shown in Figs. A1–A3.

2) External Comparison With GNSS ZTD as a Reference: We further examined the external accuracy of tropospheric delays derived from ERA5 with different layers with GNSS measurements as a reference. Not all tropospheric delay parameters (see Table V) have corresponding measured data references, and ground-based GNSS measurements yield only ZTD, Gn, and Ge. We selected the data from 338

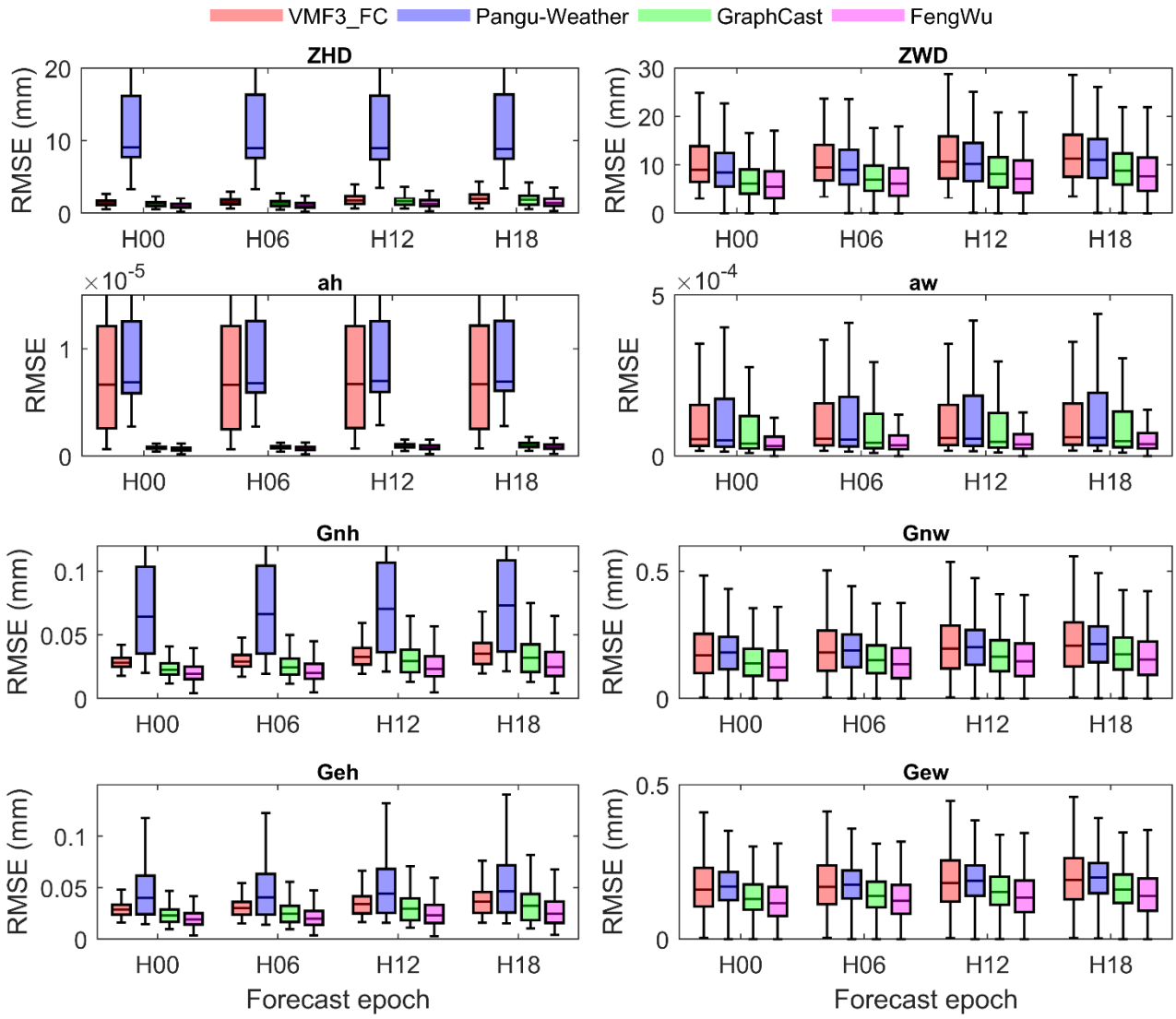

Fig. 4. RMSE of global zenith delays (ZHD and ZWD), mapping functions (ah and aw), and gradients (Gnh, Gnw, Geh, and Gew) derived from VMF3_FC, Pangu-Weather, GraphCast, and FengWu FMs. Note that due to the spatial inhomogeneity of the grid, the above RMSE is latitude-weighted, and the different forecast epoch corresponds to different forecast lengths, as shown in Table III.

GNSS stations (stations were selected according to a threshold of more than 95% data completeness as proposed by Ding et al. [62]) and calculated the bias and RMSE of ZTD, Gn, Ge, with the results depicted in Table VI. Table VI shows that the accuracy of the gradients is essentially unaffected by the number of layers and that the ZTD difference between the 25- and 37-levels is rather small. The RMSE is almost 1 cm for each, while the 13-level results were almost 2 cm. This result suggests that it is preferable to use NWMs with 25 layers and above in high-precision tropospheric delay calculations to avoid introducing errors. The distribution of the 338 GNSS stations that participated in the statistical results in Table VI, as well as their BIAS and RMSE, is shown in Figs. A4–A6. In addition, as of July 2024, additional FMs, such as ClimaX, CliMA, FuXi, and AIFS, have emerged; however, none support 37-layer pressure level inputs, and GraphCast and FengWu are the only two models that do not introduce additional errors due to the number of pressure level.

B. Comparison With Grid-Wise Model Products

In evaluating the precision and longevity of highly precise tropospheric delays produced from the AI FMs, it is important to consider the potential diminishing forecast model precision with forecast length. To assess this, we computed and analyzed the RMSE of the Pangu-Weather and GraphCast forecasts for 15 days, using the ERA5 37-level tropospheric delay as a reference. We also included the empirical model GPT3 and discrete product VMF3_FC in the comparison at the same forecast length to examine the benefits of the AI results over the current forecast scheme.

1) Comparison With Empirical Model GPT3: Empirical modeling, which relies on position and time as inputs to determine tropospheric delays, is widely utilized for real-time remote sensing applications, especially in the absence of prediction products. In our analysis, we utilized the results of the empirical model GPT3 as a control and calculated the RMSEs of zenith delays, mapping functions, gradients, and

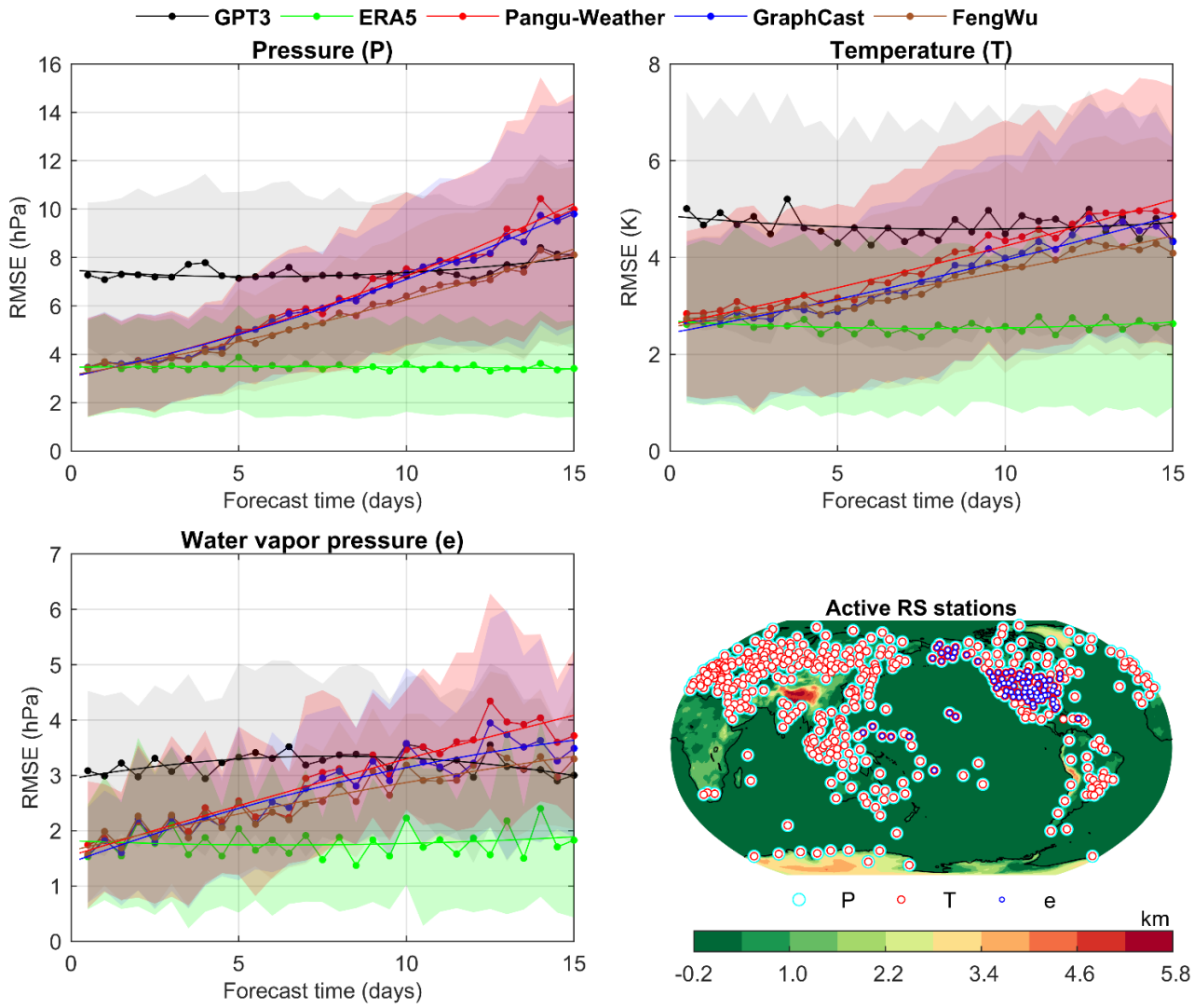

Fig. 5. RMSE of pressure (P), temperature (T), and water vapor pressure (e) from ERA5, empirical model GPT3, Pangu-Weather, GraphCast, and FengWu FMs for 15-day (60 steps, step length is 6 h) forecasts on 457 IGRA2 RS sites, with in situ RS measurements as a reference. The solid lines in the figure show the fit of the scatter and the translucent areas represent the uncertainty (standard deviation) of the values. The bottom-right subplot shows the distribution of the RS stations involved in the calculation.

surface meteorological parameters for the AI model forecasts over a 15-day period. The results are presented in Fig. 3.

Our findings show that the RMSE of the tropospheric parameters from AI models increases with the forecast length and eventually approaches or exceeds that of GPT3. The RMSE of the Pangu-Weather scheme is greater than that of the GraphCast and FengWu schemes for all forecast lengths and parameters. This is attributed to the fact that Pangu-Weather outputs only 13 layers of maximum pressure level, limiting its accuracy. Both GraphCast and FengWu are AI models that support the maximum 37-layer pressure level, and FengWu outperforms GraphCast in all the comparisons of tropospheric parameters. The RMSE of FengWu forecasts is significantly smaller than that of GraphCast, especially after the forecast length exceeds seven days. Overall, the wet part of all tropospheric delay parameters degrades faster than the hydrostatic part, and the gradient parameters also degrade faster than other parameters.

We also observed jagged fluctuations in the RMSEs of Pangu-Weather for certain tropospheric delay parameters, particularly Gnw, Gew, T, and e. This is due to the use of different sets of forecasting parameters with varying time intervals (1, 3, 6, and 24 h, with only 6 and 24 h used in this research, see Table III), and the greedy algorithm employed by Pangu-Weather to minimize error accumulation. Therefore, the accuracy is better at a forecast length of 24 h and multiples thereof. The fluctuations are more pronounced in the wet part of the tropospheric delay parameters, indicating that errors due to water vapor changes are more likely to accumulate.

2) Comparison With Discrete Model VMF3_FC: The utilization of AI FMs to obtain tropospheric delays offers the advantage of being able to generate a 15-day global forecast within minutes, provided that sufficient processing resources, such as one Nvidia V100 or one TPUv4, are available. To determine whether the forecast results are more accurate than those of existing products, we used the ERA5 results as

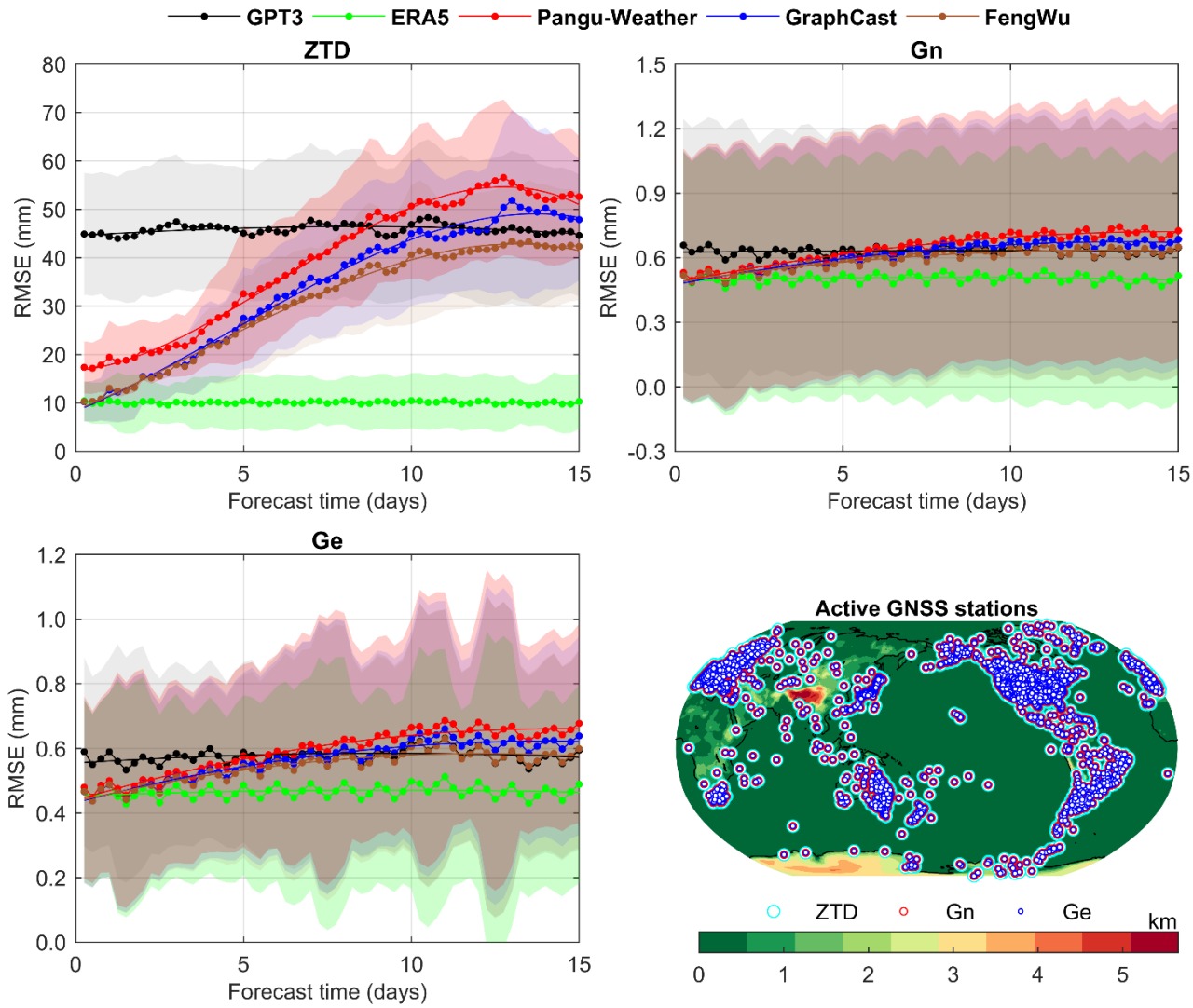

Fig. 6. RMSE of ZTD, Gn, and Ge from the Pangu-Weather, GraphCast, and FengWu FMs for 15-day (60 steps, step length is 6 h) forecasts, and ERA5 and GPT3 empirical model on 8323 NGL GNSS sites, with ground-based GNSS measurements as references. The solid lines in the figure show the RMSE values of the forecasts and the translucent area represents the uncertainty (standard deviation) of these values. The bottom-right subplot shows the distribution of the GNSS stations involved in the calculation.

a reference to calculate the RMSEs of Pangu-Weather, GraphCast, FengWu, and VMF3_FC. The results are presented in Fig. 4, and the global distribution of RMSE for each parameter under different forecast models is shown in Figs. A9–A12. It is important to note that the VMF3_FC product's most recent year is restricted to authorized users only; thus, we selected data for the entire year 2022. In addition, the different hours of each day of the VMF3_FC products correspond to different forecasting hours, with details provided in Table III.

Fig. 4 displays subplots showing the zenith delay, mapping function coefficients, north gradient, and east gradient, with the left panels representing the hydrostatic part and the right panels representing the wet part. Each subplot is further divided into four groups (H00, H06, H12, and H18) based on the forecast length, with different models represented by different colors. The comparison reveals that in the hydrostatic part, Pangu-Weather exhibits lower accuracy than VMF3_FC in zenith delay, mapping function, and gradients, particularly in zenith delay where the RMSE of Pangu-Weather is significantly higher. This is attributed to the limited number of pressure-levels in Pangu-Weather, particularly the absence of pressure layers above 50 hPa (see Table II). GraphCast and FengWu demonstrate superior accuracy in computing mapping function coefficients, indicating their strength in capturing atmospheric structural details. The comparison of the wet part is more consistent, with a relatively small difference between the four models, as the missing pressure levels in the Pangu-Weather model are primarily in the upper atmosphere where there is minimal water vapor. Overall, FengWu surpasses GraphCast, while they both outperform the traditional approach VMF3_FC in all parameters. This suggests that AI schemes, such as GraphCast and FengWu, hold promise for improving the accuracy of global forecast models for tropospheric delays.

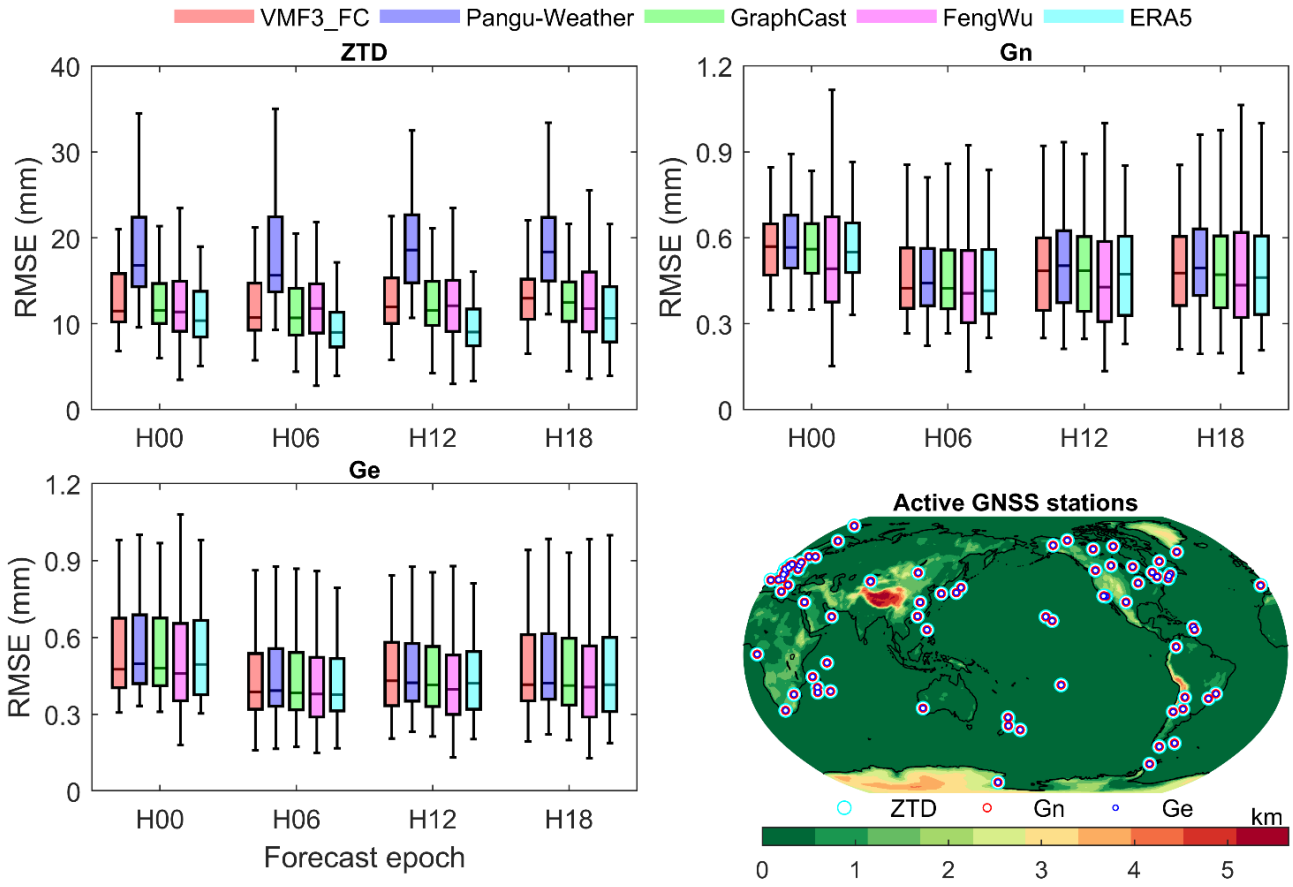

Fig. 7. RMSE of zenith tropospheric delays (ZTD), north gradient (Gn), east gradient (Ge) from VMF3_FC, Pangu-Weather, GraphCast, FengWu, and ERA5, with 88 ground-based GNSS measurements as references. The different forecast epoch corresponds to different forecast lengths, as shown in Table III. The bottom-right subplot shows the distribution of the GNSS stations involved in the calculation.

C. Comparison Using Ground-Based or In Situ Measurements as a Reference

In this section, we delve into a comprehensive comparison of the accuracy of the Pangu-Weather, GraphCast, and FengWu models for 15-day forecast durations using ground-based GNSS and in situ RS measurements as reference. In addition, we include the results from the ERA5 reanalysis data and the empirical model GPT3 for a thorough comparison and analysis. Note that the ERA5 results here all use 37 pressure levels.

1) Comparison of Meteorological Parameters Using RS Data as a Reference: The accuracy of tropospheric delay is directly impacted by the accuracy of pressure (P), temperature (T), and water vapor pressure (e), which are crucial for computing hydrostatic and wet delays. To assess the forecast outcomes, we utilized RS data for these three parameters from IGRA2 (IGRA V2) as a reference to assess the FM's forecast performance. However, the RS data are limited, with observations only twice a day and incomplete records due to various factors. After selecting more than 400 RS stations with complete data at each forecast length, we analyzed the RMSEs of pressure, temperature, and water vapor pressure computed by each model. The distribution of these stations is shown in Fig. 5, with the majority containing pressure and temperature data, and only around 50 stations also containing water vapor pressure records. Note that the original record in the RS record is relative humidity, which we converted to water vapor pressure by obtaining saturated water vapor pressure via the Wexler formulation with new coefficients adjusted for ITS-90 [63], [64], [65].

The variation of the RMSEs of pressure, temperature, and water vapor pressure computed by each model with forecast length is depicted in the top and bottom left of Fig. 5. The results show that the RMSEs of pressure, temperature, and water vapor pressure for the empirical model GPT3 and reanalysis data ERA5 remain stable. The RMSEs of P, T, and e for ERA5 are about 3.4 hPa, 2.5 K, and 1.8 hPa, respectively, and the RMSEs of P, T, and e for GPT3 are about 7.3 hPa, 4.8 K, and 3.3 hPa, respectively. On the other hand, the FM's RMSEs and uncertainties for pressure, temperature, and water vapor pressure increase as the forecast length grows. In the accuracy comparison of all three parameters, FengWu is better than GraphCast, which in turn outperforms Pangu-Weather. Especially for the pressure, the accuracy of FengWu is much higher than the other two. It is worth noting that in the comparison of temperature, the results of FengWu are still better than GPT3 for the 15-day forecast. As the forecast length increases, the uncertainty of the AI results grows,

becoming comparable or even greater than the GPT3 model for medium-term forecasts.

2) Comparison of Tropospheric Delay Parameters Using GNSS Data as a Reference: The GNSS troposphere products offer accurate ZTD measurements, in addition to the northward gradient Gn and eastward gradient Ge. In our study, we evaluated the accuracy of Pangu-Weather, GraphCast, and FengWu forecasts using ZTD, Gn, and Ge from GNSS sites as reference data. We also included results from the empirical model GPT3 and reanalysis data ERA5 as controls. Tropospheric delays from more than 8000 GNSS stations from NGL were first downsampled to 6 h and then computed according to the same methodology as for the RS data. The distribution of selected stations is depicted in Fig. 6, along with the RMSEs of ZTD, Gn, and Ge derived from each model.

The RMSE of ZTD for GPT3 and ERA5 fluctuates around 4.6 and 1.0 cm, respectively. The RMSEs of Pangu-Weather, GraphCast, and FengWu increase with forecast length, starting from about 1.8, 1.0, and 1.0 cm at the 6-h forecast, and becoming comparable to the results of GPT3 at the forecast of about ten days. It is worth noting that FengWu, the best performer, continues to outperform GPT3 in terms of ZTD accuracy for a 15-day forecast. The uncertainties of the three AI models also increase with forecast time, but the rate of increase slows down after 12 days, indicating that weather variables may converge to a climate-averaged state on longer time scales. The gradients exhibit similar variability to ZTD, with larger uncertainties resulting in a nonsignificant increase in their RMSE with forecast length. However, after about seven days of forecasting, the AI results degrade to the level of GPT3. In addition, a daily cycle is evident in the gradient results, possibly due to the updating of the initial value of the troposphere in the NGL processing strategy for its daily products (http://geodesy.unr.edu/gps/ngl.acn.txt). In addition to being provided on grid points, VMF3_FC is also provided on more than 500 GNSS sites, and of them, 88 met the conditions of this experiment. The number of these stations is small, but they are evenly distributed globally and their results are representative. Fig. 7 shows the accuracies of VMF3_FC, Pangu-Weather, GraphCast, and FengWu with ground-based GNSS measurements as a reference. GraphCast and FengWu outperform VMF3_FC for both ZTD and gradients, while Pangu-Weather lags due to a lower number of pressure levels, although this disadvantage is less significant in the gradient comparisons.

IV. Conclusion and Perspective

In conclusion, the study presents a novel approach to forecasting tropospheric delay parameters using the AI weather forecasting FMs Pangu-Weather, GraphCast, and FengWu. The approach aims to efficiently derive forecasted zenith delays, mapping function coefficients, gradients, and other meteorological parameters for real-time remote sensing applications. Our study thoroughly evaluates the accuracy and precision of these forecasted parameters. The proposed scheme has the potential to generate tropospheric delay forecasts for 15 days locally for any location within minutes, marking a significant advancement in the field of atmospheric science and geodesy. Based on our investigations, the following three key findings stand out.

First, the study reveals that the AI FM Pangu-Weather, which supports only 13 pressure levels, introduces a significant error in the computed tropospheric delay, particularly in the hydrostatic component. This discrepancy is attributed to the limited number of layers. As a recommendation for future AI weather forecast models, the study proposes the utilization of a minimum of 25 layers during model training, with the ideal scenario being the use of all 37 layers for training purposes to further enhance the model accuracy.

Second, the study demonstrates that the AI schemes utilizing GraphCast and FengWu outperform the existing VMF3_FC product in terms of accuracy for all forecast durations for all tropospheric delay parameters. This finding underscores the potential of AI FMs to provide high-precision mid-range forecasts of tropospheric delays and to autonomously maintain their precision, which is a significant advancement in the field of atmospheric science and remote sensing.

Third, the study reveals that the accuracy of tropospheric delay forecasts from the AI scheme declines to a level comparable to that of the empirical model GPT3 after about ten days. This finding, valid for about half of the parameters, suggests that while the AI scheme offers substantial improvements in forecast accuracy, there are limitations to the forecast length, and it is recommended that remote sensing users only rely on forecasts within ten days for best accuracy.

The proposed scheme surpasses existing tropospheric delay forecasting products in terms of both forecast length and precision, with potential benefits for various microwave-based real-time applications, particularly in geodesy and remote sensing. Furthermore, as AI technology continues to improve, the advantage in prediction performance of our scheme is expected to strengthen, offering even greater potential for advancements in atmospheric science and remote sensing applications. We recommend replacing the generation method of existing tropospheric delay forecast products with our scheme to eliminate the limitations of network transmission rates and computational resources. However, it is important to note that the accuracy of forecasted tropospheric delay is still dependent on the accuracy of the initial NWM. Therefore, efforts to increase the weight of high-accuracy geodetic products in NWM generation are crucial for further enhancing the precision of tropospheric delay forecasts. In the future, the study plans to further explore the potential of AI FMs by using high-accuracy geodetic tropospheric delay products as training data and initial input, which will allow us to continue improving the precision and accuracy of our scheme.

Appendix

To help more readers better comprehend this research, we provide the following supporting materials that describe more background as well as experimental details.

A. Platforms, Software, and Algorithms

1) "FM": "FM" is a term used to describe a new paradigm for building AI systems based on a general class of models,

as outlined in a comprehensive review by Percy Liang of Stanford University and over 100 leading scholars in the field of AI. This review, titled "On the Opportunities and Risk of Foundation Models" [66], provides an in-depth overview of the current opportunities and challenges of large-scale pretrained models, and the term " FM" is adopted from this work.

2) Open-Source Ray-Tracing Software RADIATE: RADIATE is an open-source ray-tracing software package, developed by the Vienna University of Technology, and the latest VMF3 products are currently generated by this software [16], [26]. Program RADIATE uses the Euler radius of curvature and the gravity acceleration is determined by the more accurate Kraus formula [67]. More than half of the baselines have a better baseline length repeatability (BLR) at submillimeter difference compared to the NSSA GSFC ray-tracing software [26]. This research performs ray tracing using the modified RADIATE software to achieve efficient processing of the data-heavy NWM in experiments [62], [68].

The NWM used for the experiments is capable of providing pressure level data up to 1 hPa, and results for locations below 1 hPa need to be extrapolated. RADIATE uses increment intervals ranging from 10 to 500 m at different heights according to Rocken et al. [69] for the vertical interpolation. The upper limit for vertical interpolation is where the atmospheric density is zero, i.e., where the refractive index is almost exactly 1 [70]. RADIATE sets this upper limit at 84 km, which is taken from the U.S. Standard Atmosphere 1976 [71]. This altitude is almost twice as high as the altitude at which the 1-hPa pressure-level atmosphere is located, and it is high enough to cover the entire neutral atmosphere.

The acquisition of mapping functions and gradients requires the use of NWM for ray-tracing. In RADIATE, the meteorological parameters at the station locations are obtained by interpolation (both interpolation and extrapolation), where the pressure is interpolated according to the exponential method of Wallace and Hobbs [72], Kleijer [73], and Nafisi et al. [70]; temperature is interpolated according to the liner method of Nafisi et al. [70] and Hobiger et al. [74]; and water vapor pressure is interpolated according to the exponential method of Böhm et al. [75]. The reasons why these methods were chosen and other detailed descriptions can be found in [76] (https://www.vlbi.at/data/publications/2016_hofmeister_thesis.pdf).

3) Evaluation Metrics: In this research, the evaluation of the model tropospheric parameters is conducted using the RMSE. In addition, the ACC is employed to gauge the level of agreement between the model predictions and observed data. The ACC, commonly utilized in the assessment of climate or weather models, serves as a reliable measure of accuracy. A higher ACC value, approaching 1, signifies a more precise prediction. To ensure accuracy in the calculations, both RMSE and ACC incorporate latitudinal weighting. This is essential because the spatial distribution of latitudinal and longitudinal grid points across the Earth's surface is not homogenous. The computation of these two metrics is outlined as follows:

$$\mathrm{RMSE}(v) = \sqrt{\frac{\sum_{i=1}^{N_{\mathrm{lat}}}\sum_{j=1}^{N_{\mathrm{lon}}} P(i)\left(\mathbf{A}_{i,j}^{v}-\mathbf{B}_{i,j}^{v}\right)}{N_{\mathrm{lat}}\times N_{\mathrm{lon}}}} \tag{A1}$$

$$\mathrm{ACC}(v) = \frac{\sum_{i=1}^{N_{\mathrm{lat}}}\sum_{j=1}^{N_{\mathrm{lon}}} P(i)\mathbf{A}_{i,j}^{v}\mathbf{B}_{i,j}^{v}}{\sqrt{\sum_{i=1}^{N_{\mathrm{lat}}}\sum_{j=1}^{N_{\mathrm{lon}}} P(i)\left(\mathbf{A}_{i,j}^{v}\right)^2 \times \sum_{i=1}^{N_{\mathrm{lat}}}\sum_{j=1}^{N_{\mathrm{lon}}} P(i)\left(\mathbf{B}_{i,j}^{v}\right)^2}} \tag{A2}$$

where v is any tropospheric parameters; $A_{i,j}^{v}$ and $B_{i,j}^{v}$ are the two latitude/longitude grid sequences used for the comparison, respectively; and $P(i)$ is the weights, and it is defined as follows:

$$P(i) = N_{\mathrm{lat}} \times \frac{\cos\phi_i}{\sum_{i'=1}^{N_{\mathrm{lat}}}\cos\phi_{i'}} \tag{A3}$$

where ϕ_i is the latitude of the grid point. The RMSEs and ACCs displayed in Figs. A7 and A8 are calculated by weighted averaging the aforementioned equations, and they represent the RMSEs and ACCs of the global grid series at a specific epoch moment. In contrast, the RMSEs displayed in other figures are the RMSEs of the time series at each site.

4) Relationships Between Tropospheric Delay Parameters: The tropospheric delay parameters that appear in this research include meteorological parameters (pressure, temperature, and water vapor pressure), zenith delay (ZHD and ZWD), mapping function (ah and aw), and gradients (Gnh, Gnw, Geh, and Gew). These parameters are briefly described as follows.

Due to different atmospheric compositions, the refractivity of a radio wave traveling through any position in space is different. The refractivity N can be determined according to Smith and Weintraub [77] as

$$N = k_1\frac{p_d}{T} + k_2\frac{p_w}{T} + k_3\frac{p_w}{T^2} \tag{A4}$$

where p_d and p_w are the partial pressure of dry air in hPa and the partial pressure of water vapor in hPa, respectively; T is the temperature in kelvin. The variables k_1–k_3 denote refractivity coefficients determined by numerous different laboratory measurements [2], and they are equal to 77.6890, 71.2952, and 375 463 K/hPa, respectively, according to Rueger [78] and [79].

The refractivity N can be divided into a hydrostatic part N_h and a nonhydrostatic part N_w (the wet part)

$$N = N_h + N_w. \tag{A5}$$

The hydrostatic refractivity is mainly related to the total pressure; the wet refractivity is mainly related to the water vapor pressure. The hydrostatic delay in the zenith direction (ZHD) and the wet delay in the zenith direction (ZWD) can be obtained by the following integrals [2]:

$$\mathrm{ZHD} = 10^{-6}\int_{h_0}^{\infty} N_h(z)dz \tag{A6}$$

$$\mathrm{ZWD} = 10^{-6}\int_{h_0}^{\infty} N_w(z)dz \tag{A7}$$

where h_0 is the station height.

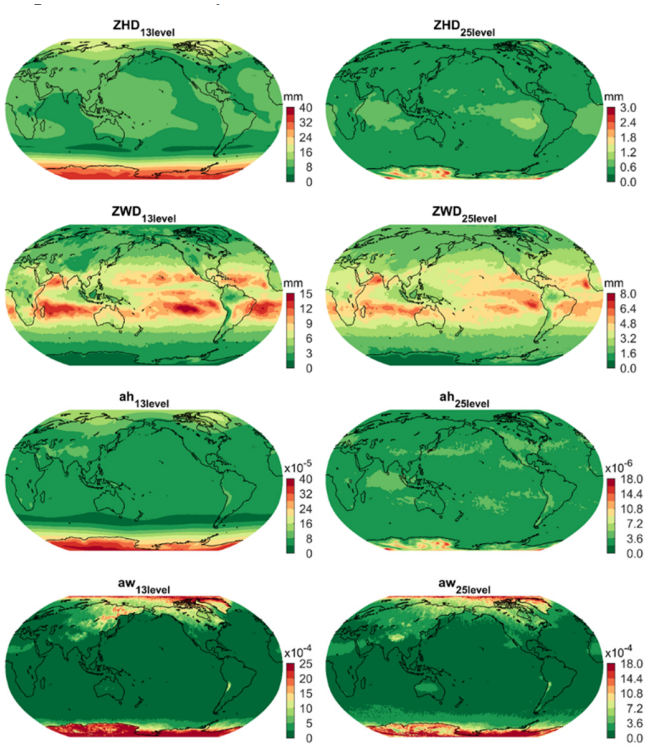

Fig. A1. RMSE of ZHD/ZWD/ah/aw derived from 13-pressure level ERA5 and 25-pressure level ERA5 data with 37-pressure level ERA5 data as a reference at grid-wise VMF3 of 1° ×1° horizontal resolutions (00z, 06z, 12z, and 18z hours on every day in 2022). Note the different color bar scales of the panels.

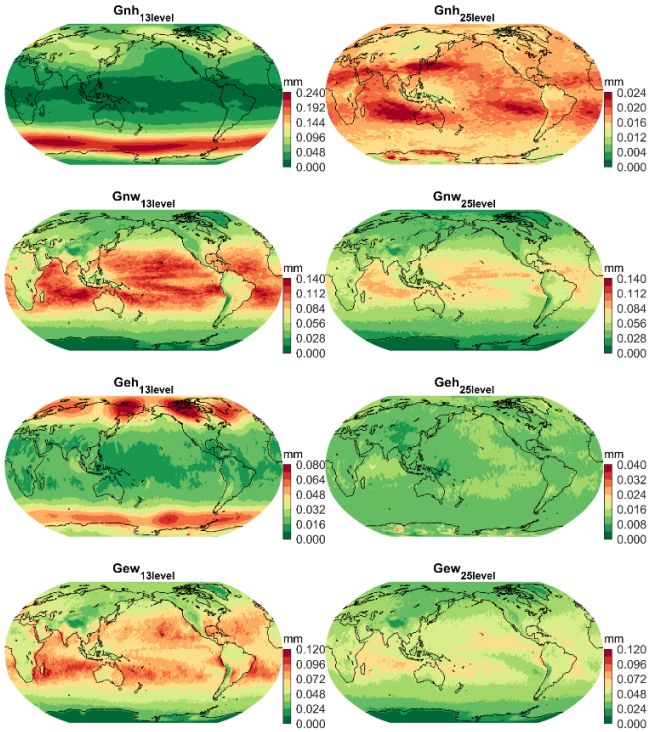

Fig. A2. RMSE of tropospheric gradients derived from 13-pressure level ERA5 and 25-pressure level ERA5 data with 37-pressure level ERA5 data as a reference at grid-wise VMF3 of 1° × 1° horizontal resolutions (00z, 06z, 12z, and 18z hours on every day in 2022). Note the different color bar scales of the panels.

Chen and Herring [80] proposed the following formula for the troposphere delays:

$$\Delta L(\alpha, \varepsilon) = \Delta L_0(\varepsilon) + mf_g(\varepsilon) \cdot [G_n \cdot \cos(\alpha) + G_e \cdot \sin(\alpha)] \tag{A8}$$

where α and ε are azimuth and elevation angles respectively, $\Delta L_0\ (\varepsilon)$ is the isotropic part:

$$\Delta L_0(\varepsilon) = \mathrm{ZHD} \cdot mf_h(\varepsilon) + \mathrm{ZWD} \cdot mf_w(\varepsilon) \tag{A9}$$

where mf_h and mf_w are hydrostatic and wet mapping function, respectively. The mapping function is built based on three coefficients a, b, and c

$$mf(\varepsilon) = \frac{1 + \frac{a}{1+\frac{b}{1+c}}}{\sin(\varepsilon) + \frac{a}{\sin(\varepsilon)+\frac{b}{\sin(\varepsilon)+c}}} \tag{A10}$$

where the coefficient a is the determining part, while b and c are usually set to empirical values. The mapping functions ah and aw in this research are the hydrostatic and wet parts of coefficients a, respectively.

Following $\Delta L_0(\varepsilon)$ is the anisotropic part of $\Delta L(\alpha, \varepsilon)$, and G_n and G_e are the north gradient and east gradient, respectively. The mapping function of gradient can be written as

$$mf_g(\varepsilon) = \frac{1}{\sin(\varepsilon) \cdot \tan(\varepsilon) + C}. \tag{A11}$$

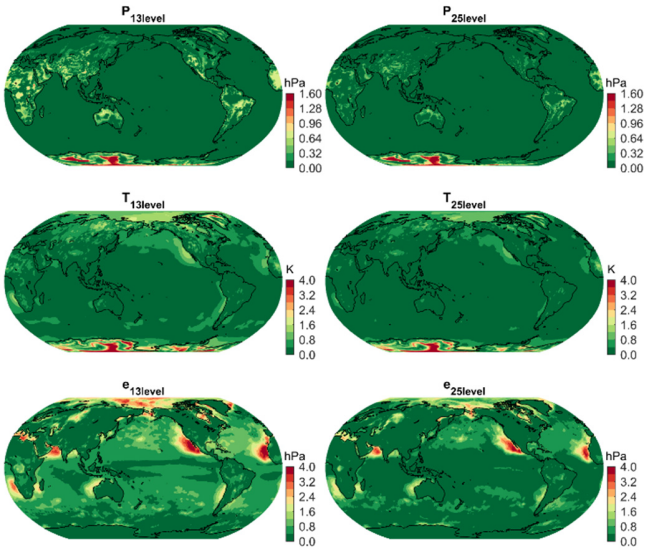

Fig. A3. RMSE of meteorological parameters derived from 13-pressure level ERA5 and 25-pressure level ERA5 data with 37-pressure level ERA5 data as a reference at grid-wise VMF3 of 1° × 1° horizontal resolution (00z, 06z, 12z, and 18z hours on every day in 2022). Note the different color bar scales of the panels.

The gradient mapping function coefficient C can be written as

$$C = \frac{3H}{R_e} \tag{A12}$$

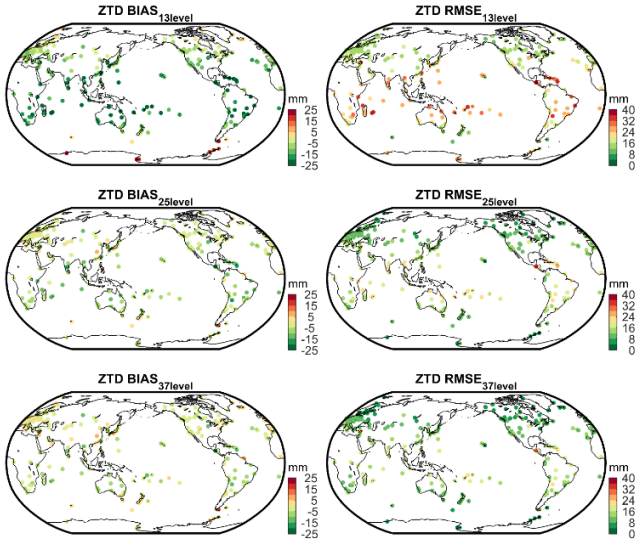

Fig. A4. Mean bias (BIAS) and RMSE of ZTD derived from 13-/25-/37-pressure level ERA5 data with GNSS data as a reference at 338 NGL stations (daily at 00z, 06z, 12z, and 18z in 2022).

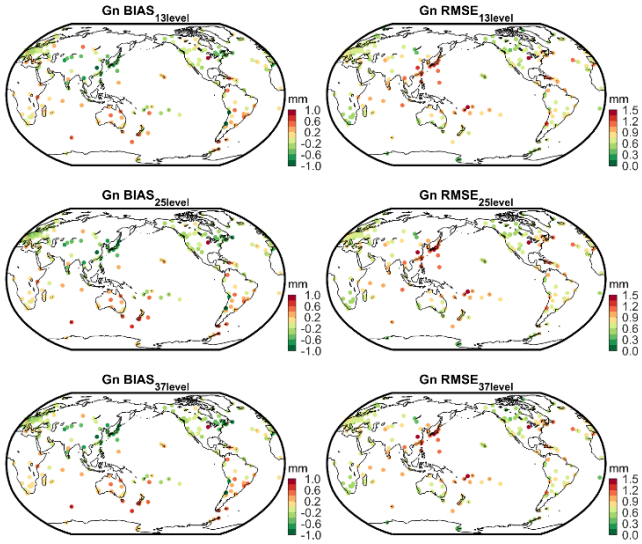

Fig. A5. Mean bias (BIAS) and RMSE of Gn derived from 13-/25-/37-pressure level ERA5 data with GNSS data as a reference at 338 NGL stations (daily at 00z, 06z, 12z, and 18z in 2022).

where R_e is the Erath radius and H is the height of the neutral atmosphere assuming constant density with height and conservation of the total mass [2]. Chen and Herring [80] get values of $C_h = 0.0031$ and $C_w = 0.0007$ for the gradient mapping function coefficient.

B. Experimental Details

1) Global Distribution (Grid-Wise) of RMSE of Different Pressure-Level Layers: We compare the differences in tropospheric delay parameters calculated from NWMs with different pressure-level layers in Section III-A. Since comparing the differences is not among the most important tasks of this study, only the final statistical result is given in the main text, which represents a global average. We give the global distribution of

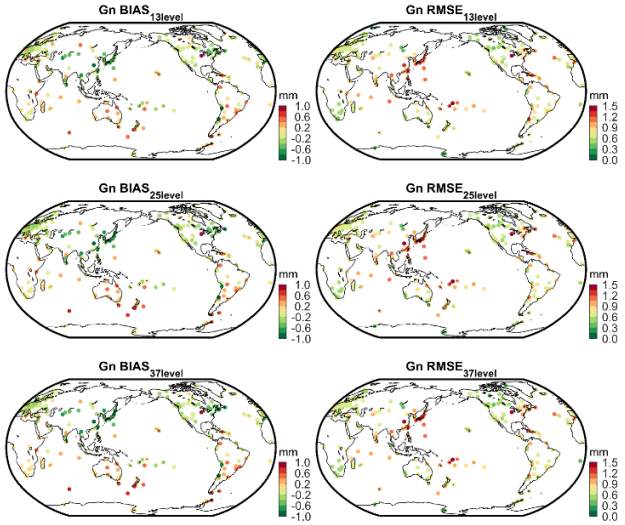

Fig. A6. Mean bias (BIAS) and RMSE of Ge derived from 13-/25-/37-pressure level ERA5 data with GNSS data as reference at 338 NGL stations (daily at 00z, 06z, 12z, and 18z in 2022).

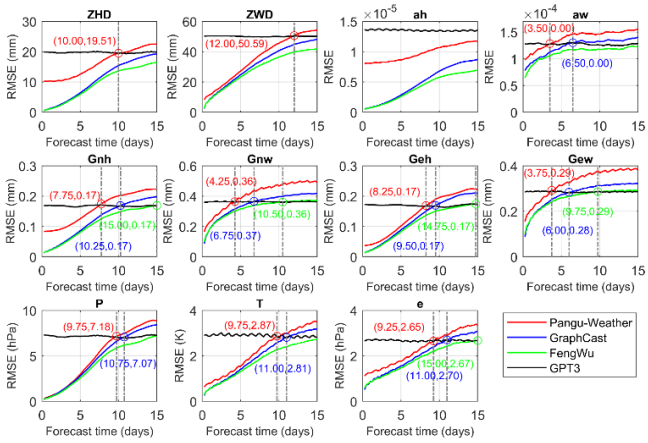

Fig. A7. RMSE of global zenith delays (ZHD and ZWD), mapping functions (ah and aw), gradients (Gnh, Gnw, Geh, and Gew), pressure (P), temperature (T), and water vapor pressure (e) from the Pangu-Weather, GraphCast, and FengWu FM for 15-day (60 steps, times of 00z, 06z, 12z, and 18z) forecasts and GPT3 empirical model on $1^\circ \times 1^\circ$ grid. Note that due to the spatial inhomogeneity of the grid, the above RMSE is latitude-weighted.

the differences in the number of layers for different parameters in Figs. A1–A3. Readers, especially those who perform AI weather forecasting, may be able to get enlightening information from this for improving the selection of layers for training data, as well as focusing on optimization specifically for regions with poorer accuracy. Since tropospheric delays reflect the cumulative effects of all meteorological data layers combined, they may be better indicators of model performance than the evaluations in existing papers on AI base models that only result in some individual pressure-level.

2) Global Distribution (Site-Wise) of RMSE of Different Pressure-Level Layers: GNSS is one of the technologies with the highest accuracy in obtaining ZTD, and accuracy assessments referenced to measurements from GNSS stations are more reliable and robust at the station location than results from ERA5. We give in Figs. A4–A6 the global distribution

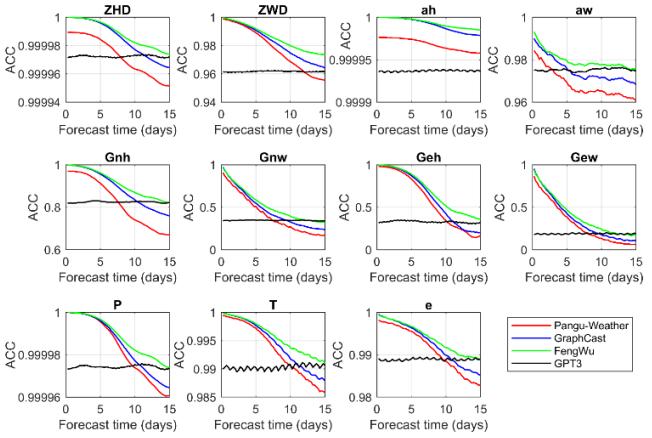

Fig. A8. ACC of global zenith delays (ZHD and ZWD), mapping functions (ah and aw), gradients (Gnh, Gnw, Geh, and Gew), pressure (P), temperature (T), and water vapor pressure (e) from the Pangu-Weather, GraphCast, and FengWu FM for 15-day (60 steps, times of 00z, 06z, 12z, and 18z) forecasts and GPT3 empirical model on $1^\circ \times 1^\circ$ grid. An ACC value close to 1 indicates a higher correlation between forecast anomalies and actual anomalies.

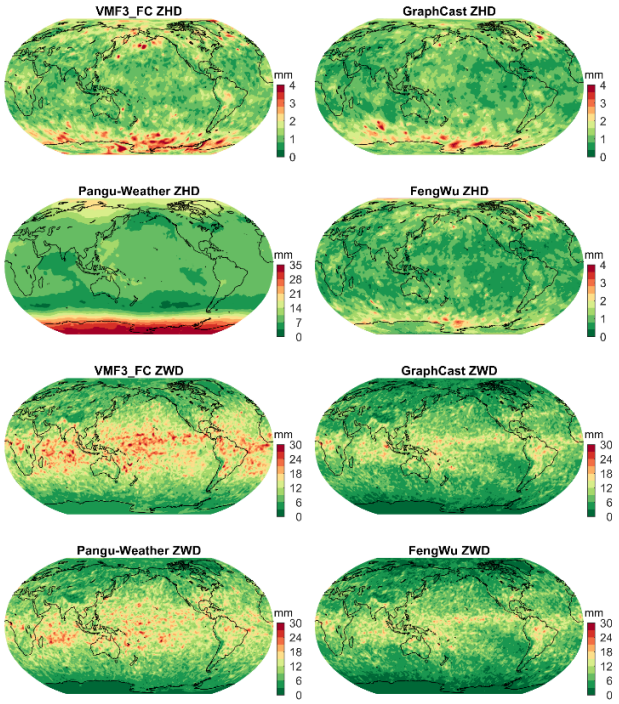

Fig. A9. Comparison of VMF3_FC, Pangu-Weather, GraphCast, and FengWu zenith tropospheric delay accuracy. Note the different color bar scales of the panels.

of the BIAS and RMSE results for the 338 GNSS stations participating in the assessment.

3) RMSE and ACC of Tropospheric Delay Parameters of 15-Day Forecasting: Note that there are two different algorithms for RMSE in this research. The first algorithm, which is shown in Eq. (A1), is to compute the weighted RMSE between two different grids and then calculate the average at different epochs to get the average RMSE. This algorithm is the one that has been used in the field of weather forecasting, and it is also the method used by AI FMs such as Pangu-Weather, and this method is unified with ACC. The other is the RMSE

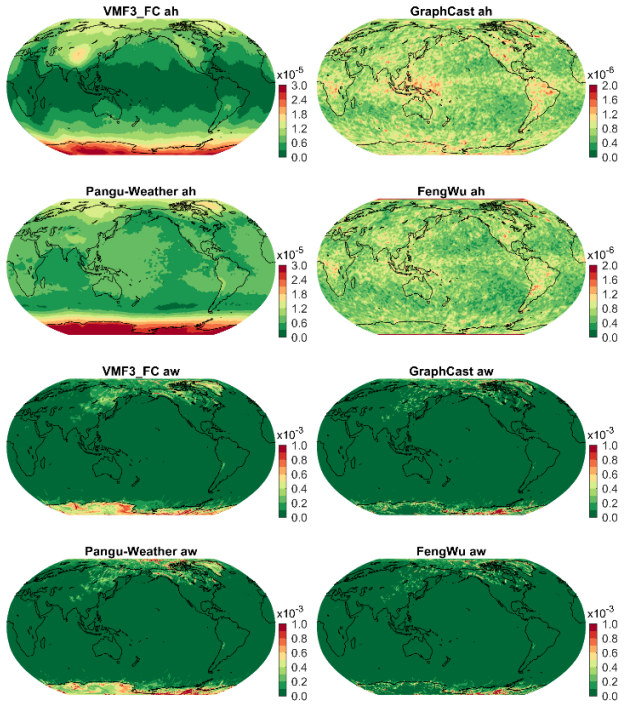

Fig. A10. Comparison of VMF3_FC, Pangu-Weather, GraphCast, and FengWu mapping function accuracy. Note the different color bar scales of the panels.

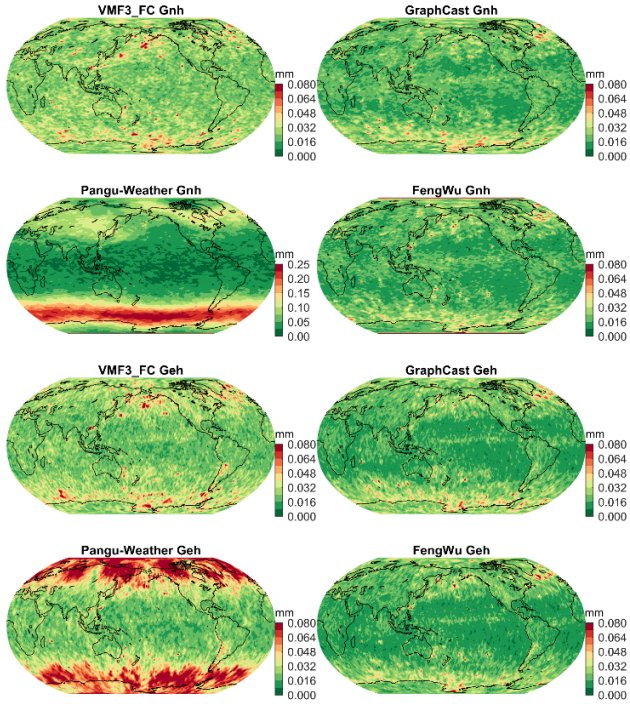

Fig. A11. Comparison of VMF3_FC, Pangu-Weather, GraphCast, and FengWu hydrostatic gradient accuracy. Note the different color bar scales of the panels.

in the field of geodesy, which is to find the RMSE between two time series of points on each grid point and then do a latitude-weighted average of these grid point RMSEs, which is the method used for the plots in the main text. We put the results calculated by the first method next [see Fig. A7 (RMSE) and Fig. A8 (ACC)].

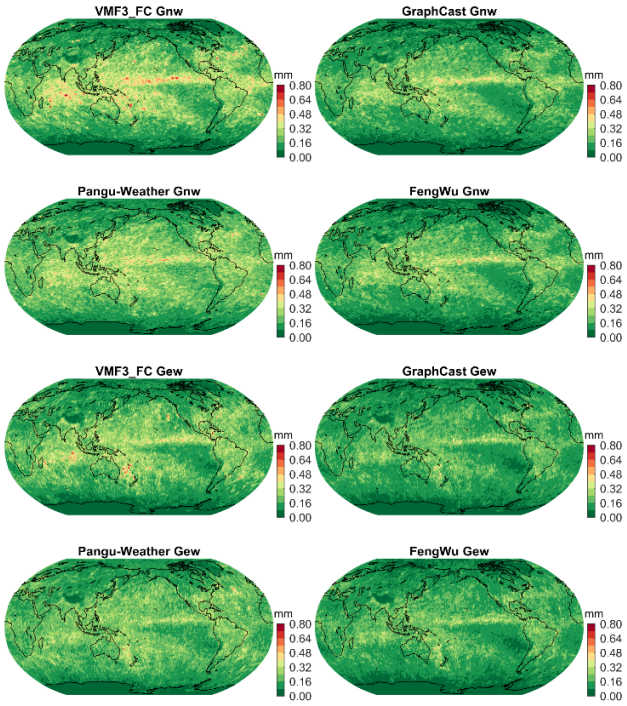

Fig. A12. Comparison of VMF3_FC, Pangu-Weather, GraphCast, and FengWu wet gradient accuracy. Note the different color bar scales of the panels.

4) Comparison of GraphCast and VMF3_FC Precision: In the comparison in Section III-B2, GraphCast and FengWu comprehensively outperforms VMF3_FC from the global mean scale in all parameters. We give in Figs. A9–A12 the differences between the four types of models for forecasting 24 h results. Information about Pangu-Weather, GraphCast and FengWu comparison with VMF3_FC, the main areas of improvement, etc. can be obtained from Figs. A9–A12.

ACKNOWLEDGMENT

This research processed more than 28 Tb of data. The authors would like to thank the European Centre for Medium-Range Weather Forecasts (ECMWFs) for providing the ERA5 data on pressure levels (https://cds.climate.copernicus.eu/cdsapp#!/dataset/reanalysis-era5-pressure-levels?tab=overview) and ERA5 data on single levels (https://cds.climate.copernicus.eu/cdsapp#!/dataset/reanalysis-era5-single-levels?tab=form), Nevada Geodetic Laboratory (NGL) for providing Global Navigation Satellite System (GNSS) tropospheric delay products (http://geodesy.unr.edu/gps_timeseries/trop/), National Oceanic and Atmospheric Administration (NOAA) for providing Integrated Global Radiosonde Archive (IGRA2) RS data. They would like to thank Huawei Cloud for providing the open-source foundation model (FM) Pangu-Weather (https://github.com/198808xc/Pangu-Weather), Google DeepMind for providing weather forecast model GraphCast (https://github.com/google-deepmind/graphcast), and Shanghai AI Lab for providing weather forecast model FengWu (https://github.com/OpenEarthLab/FengWu). In addition, they would also like to thank the Technische Universität Wien for the open-source ray-tracing software RADIATE (https://github.com/TUW-VieVS/RADIATE) and ecmwf-lab for open-source AI models command-line management tool ai-models (https://github.com/ecmwf-lab/ai-models).

REFERENCES

[1] G. Elgered, "Tropospheric radio-path delay from ground-based microwave radiometry," in *Atmospheric Remote Sensing by Microwave Radiometry*, M. Janssen, Ed., New York, NY, USA: Wiley, 1993, ch. 5, pp. 215–258.

[2] T. Nilsson, J. Böhm, D. D. Wijaya, A. Tresch, V. Nafisi, and H. Schuh, "Path delays in the neutral atmosphere," in *Atmospheric Effects in Space Geodesy*, J. Böhm and H. Schuh, Eds., Berlin, Germany: Springer, 2013, pp. 73–136, doi: 10.1007/978-3-642-36932-2_3.

[3] M. Drożdżewski and K. Sośnica, "Satellite laser ranging as a tool for the recovery of tropospheric gradients," *Atmos. Res.*, vol. 212, pp. 33–42, Nov. 2018, doi: 10.1016/j.atmosres.2018.04.028.

[4] T. A. Herring, "Modeling atmospheric delays in the analysis of space geodetic data," in *Proc. Symp. Refraction Trans. Atmos. Signals Geodesy*, J. C. de Munck and T. A. T. Spoelstra, Eds., 1992, pp. 157–164.

[5] A. B. O. Jensen and O. Ovstedal, "The effect of different tropospheric models on precise point positioning in kinematic mode," *Surv. Rev.*, vol. 40, no. 308, pp. 173–187, Apr. 2008, doi: 10.1179/003962608x290979.

[6] X. Hua, C. Pan, Y. Shi, J. Liu, and H. Hong, "Removing atmospheric turbulence effects via geometric distortion and blur representation," *IEEE Trans. Geosci. Remote Sens.*, vol. 60, 2022, Art. no. 4100113, doi: 10.1109/TGRS.2020.3043627.

[7] A. van der Hoeven, R. F. Hanssen, and B. Ambrosius, "Tropospheric delay estimation and analysis using GPS and SAR interferometry," *Phys. Chem. Earth, Parts A/B/C*, vol. 27, nos. 4–5, pp. 385–390, Jan. 2002, doi: 10.1016/s1474-7065(02)00016-5.

[8] L. Yang, J. Wang, H. Li, and T. Balz, "Global assessment of the GNSS single point positioning biases produced by the residual tropospheric delay," *Remote Sens.*, vol. 13, no. 6, p. 1202, Mar. 2021, doi: 10.3390/rs13061202.

[9] J. L. Awange, "Environmental monitoring using GNSS: Global navigation satellite systems," in *Environmental Science and Engineering*. Berlin, Germany: Springer, 2012, doi: 10.1007/978-3-540-88256-5.

[10] C. Albergel et al., "ERA-5 and ERA-interim driven ISBA land surface model simulations: Which one performs better?" *Hydrol. Earth Syst. Sci.*, vol. 22, no. 6, pp. 3515–3532, Jun. 2018, doi: 10.5194/hess-22-3515-2018.

[11] P. Yuan et al., "Characterisations of Europe's integrated water vapour and assessments of atmospheric reanalyses using more than 2 decades of ground-based GPS," *Atmos. Chem. Phys.*, vol. 23, no. 6, pp. 3517–3541, Mar. 2023, doi: 10.5194/acp-23-3517-2023.

[12] P. Yuan et al., "Feasibility of ERA5 integrated water vapor trends for climate change analysis in continental Europe: An evaluation with GPS (1994–2019) by considering statistical significance," *Remote Sens. Environ.*, vol. 260, Jul. 2021, Art. no. 112416, doi: 10.1016/j.rse.2021.112416.

[13] P. Yuan et al., "An enhanced integrated water vapour dataset from more than 10 000 global ground-based GPS stations in 2020," *Earth Syst. Sci. Data*, vol. 15, no. 2, pp. 723–743, Feb. 2023, doi: 10.5194/essd-15-723-2023.

[14] J. Boehm, R. Heinkelmann, and H. Schuh, "Short note: A global model of pressure and temperature for geodetic applications," *J. Geodesy*, vol. 81, no. 10, pp. 679–683, Oct. 2007, doi: 10.1007/s00190-007-0135-3.

[15] J. Böhm, G. Möller, M. Schindelegger, G. Pain, and R. Weber, "Development of an improved empirical model for slant delays in the troposphere (GPT2w)," *GPS Solutions*, vol. 19, no. 3, pp. 433–441, Jul. 2015, doi: 10.1007/s10291-014-0403-7.

[16] D. Landskron and J. Böhm, "VMF3/GPT3: Refined discrete and empirical troposphere mapping functions," *J. Geodesy*, vol. 92, no. 4, pp. 349–360, Apr. 2018, doi: 10.1007/s00190-017-1066-2.

[17] J. Boehm, B. Werl, and H. Schuh, "Troposphere mapping functions for GPS and very long baseline interferometry from European centre for medium-range weather forecasts operational analysis data," *J. Geophys. Res., Solid Earth*, vol. 111, no. B2, Feb. 2006, Art. no. 2005JB003629, doi: 10.1029/2005jb003629.

[18] J. Boehm, J. Kouba, and H. Schuh, "Forecast Vienna mapping functions 1 for real-time analysis of space geodetic observations," *J. Geodesy*, vol. 83, no. 5, pp. 397–401, May 2009, doi: 10.1007/s00190-008-0216-y.

[19] C. Zhou, J. Wang, A. Dai, and P. W. Thorne, "A new approach to homogenize global subdaily radiosonde temperature data from 1958 to 2018," *J. Climate*, vol. 34, no. 3, pp. 1163–1183, Feb. 2021, doi: 10.1175/jcli-d-20-0352.1.

[20] J. Ding, J. Chen, W. Tang, and Z. Song, "Spatial–temporal variability of global GNSS-derived precipitable water vapor (1994–2020) and climate implications," *Remote Sens.*, vol. 14, no. 14, p. 3493, Jul. 2022, doi: 10.3390/rs14143493.

[21] M. J. Fernandes, C. Lázaro, M. Ablain, and N. Pires, "Improved wet path delays for all ESA and reference altimetric missions," *Remote Sens. Environ.*, vol. 169, pp. 50–74, Nov. 2015, doi: 10.1016/j.rse.2015.07.023.

[22] T. Vieira, M. J. Fernandes, and C. Lázaro, "An enhanced retrieval of the wet tropospheric correction for Sentinel-3 using dynamic inputs from ERA5," *J. Geodesy*, vol. 96, no. 4, p. 28, Apr. 2022, doi: 10.1007/s00190-022-01622-z.

[23] J. Foster, B. Brooks, T. Cherubini, C. Shacat, S. Businger, and C. L. Werner, "Mitigating atmospheric noise for InSAR using a high resolution weather model," *Geophys. Res. Lett.*, vol. 33, no. 16, p. 2006, Aug. 2006, doi: 10.1029/2006gl026781.

[24] Z. Zhang, Y. Lou, W. Zhang, H. Wang, Y. Zhou, and J. Bai, "Assessment of ERA-interim and ERA5 reanalysis data on atmospheric corrections for InSAR," *Int. J. Appl. Earth Observ. Geoinf.*, vol. 111, Jul. 2022, Art. no. 102822, doi: 10.1016/j.jag.2022.102822.

[25] B. Soja et al., "Tropospheric delay determination by Kalman filtering VLBI data," *Earth, Planets Space*, vol. 67, no. 1, p. 144, Dec. 2015, doi: 10.1186/s40623-015-0293-0.

[26] A. Hofmeister and J. Böhm, "Application of ray-traced tropospheric slant delays to geodetic VLBI analysis," *J. Geodesy*, vol. 91, no. 8, pp. 945–964, Aug. 2017, doi: 10.1007/s00190-017-1000-7.

[27] T. R. Emardson and P. O. J. Jarlemark, "Atmospheric modelling in GPS analysis and its effect on the estimated geodetic parameters," *J. Geodesy*, vol. 73, no. 6, pp. 322–331, Jul. 1999, doi: 10.1007/s001900050249.

[28] J. Wang et al., "Retrieving precipitable water vapor from ship-borne multi-GNSS observations," *Geophys. Res. Lett.*, vol. 46, no. 9, pp. 5000–5008, May 2019, doi: 10.1029/2019gl082136.

[29] J. Wang et al., "Improving the vertical modeling of tropospheric delay," *Geophys. Res. Lett.*, vol. 49, no. 5, Mar. 2022, Art. no. e2021GL096732, doi: 10.1029/2021gl096732.

[30] T. Nilsson et al., "Improving the modeling of the atmospheric delay in the data analysis of the intensive VLBI sessions and the impact on the UT1 estimates," *J. Geodesy*, vol. 91, no. 7, pp. 857–866, Jul. 2017, doi: 10.1007/s00190-016-0985-7.

[31] N. Takeichi, T. Sakai, S. Fukushima, and K. Ito, "Tropospheric delay correction with dense GPS network in L1-SAIF augmentation," *GPS Solutions*, vol. 14, no. 2, pp. 185–192, Mar. 2010, doi: 10.1007/s10291-009-0133-4.

[32] A. Cegla, W. Rohm, E. Lasota, and R. Biondi, "Detecting volcanic plume signatures on GNSS signal, based on the 2014 Sakurajima Eruption," *Adv. Space Res.*, vol. 69, no. 1, pp. 292–307, Jan. 2022, doi: 10.1016/j.asr.2021.08.034.

[33] A. Akilan, S. Padhy, V. P. Dimri, H. Schuh, and K. K. A. Azeez, "Co-seismic and post-seismic changes in ZTD and TEC of the 2015 Nepal earthquake," *Pure Appl. Geophys.*, vol. 178, no. 9, pp. 3339–3354, Sep. 2021, doi: 10.1007/s00024-021-02830-y.

[34] C. J. Ruhl, D. Melgar, R. Grapenthin, and R. M. Allen, "The value of real-time GNSS to earthquake early warning," *Geophys. Res. Lett.*, vol. 44, no. 16, pp. 8311–8319, Aug. 2017, doi: 10.1002/2017gl074502.

[35] Y. G. Ejigu, F. N. Teferle, A. Klos, J. Bogusz, and A. Hunegnaw, "Monitoring and prediction of hurricane tracks using GPS tropospheric products," *GPS Solutions*, vol. 25, no. 2, p. 76, Apr. 2021, doi: 10.1007/s10291-021-01104-3.

[36] O. E. J. Wing, C. C. Sampson, P. D. Bates, N. Quinn, A. M. Smith, and J. C. Neal, "A flood inundation forecast of hurricane Harvey using a continental-scale 2D hydrodynamic model," *J. Hydrol. X*, vol. 4, Jul. 2019, Art. no. 100039, doi: 10.1016/j.hydroa.2019.100039.

[37] Z. Sun, B. Zhang, and Y. Yao, "A global model for estimating tropospheric delay and weighted mean temperature developed with atmospheric reanalysis data from 1979 to 2017," *Remote Sens.*, vol. 11, no. 16, p. 1893, Aug. 2019, doi: 10.3390/rs11161893.

[38] N. Penna, A. Dodson, and W. Chen, "Assessment of EGNOS tropospheric correction model," *J. Navigat.*, vol. 54, no. 1, pp. 37–55, Jan. 2001, doi: 10.1017/s0373463300001107.

[39] Y. Yao, B. Zhang, C. Xu, C. He, C. Yu, and F. Yan, "A global empirical model for estimating zenith tropospheric delay," *Sci. China Earth Sci.*, vol. 59, no. 1, pp. 118–128, Jan. 2016, doi: 10.1007/s11430-015-5173-8.

[40] P. Lynch, "The origins of computer weather prediction and climate modeling," *J. Comput. Phys.*, vol. 227, no. 7, pp. 3431–3444, Mar. 2008, doi: 10.1016/j.jcp.2007.02.034.

[41] A. J. Simmons and A. Hollingsworth, "Some aspects of the improvement in skill of numerical weather prediction," *Quart. J. Roy. Meteorolog. Soc.*, vol. 128, no. 580, pp. 647–677, Jan. 2002, doi: 10.1256/003590002321042135.

[42] J. Pathak et al., "FourCastNet: A global data-driven high-resolution weather model using adaptive Fourier neural operators," 2022, *arXiv:2202.11214*.

[43] K. Bi, L. Xie, H. Zhang, X. Chen, X. Gu, and Q. Tian, "Accurate medium-range global weather forecasting with 3D neural networks," *Nature*, vol. 619, no. 7970, pp. 533–538, Jul. 2023, doi: 10.1038/s41586-023-06185-3.

[44] R. Lam et al., "Learning skillful medium-range global weather forecasting," *Science*, vol. 382, no. 6677, pp. 1416–1421, Dec. 2023, doi: 10.1126/science.adi2336.

[45] K. Chen et al., "FengWu: Pushing the skillful global medium-range weather forecast beyond 10 days lead," 2023, *arXiv:2304.02948*.

[46] P. Bougeault et al., "The THORPEX interactive grand global ensemble," *Bull. Amer. Meteorolog. Soc.*, vol. 91, no. 8, pp. 1059–1072, Aug. 2010, doi: 10.1175/2010bams2853.1.

[47] H. Hersbach et al., "The ERA5 global reanalysis," *Quart. J. Roy. Meteorol. Soc.*, vol. 146, no. 730, pp. 1999–2049, Jul. 2020, doi: 10.1002/qj.3803.

[48] R. Urraca, T. Huld, A. Gracia-Amillo, F. J. Martinez-de-Pison, F. Kaspar, and A. Sanz-Garcia, "Evaluation of global horizontal irradiance estimates from ERA5 and COSMO-REA6 reanalyses using ground and satellite-based data," *Sol. Energy*, vol. 164, pp. 339–354, Apr. 2018, doi: 10.1016/j.solener.2018.02.059.

[49] M. Tarek, F. P. Brissette, and R. Arsenault, "Evaluation of the ERA5 reanalysis as a potential reference dataset for hydrological modelling over North America," *Hydrol. Earth Syst. Sci.*, vol. 24, no. 5, pp. 2527–2544, May 2020, doi: 10.5194/hess-24-2527-2020.

[50] H. Zhang, Y. Yuan, and W. Li, "An analysis of multisource tropospheric hydrostatic delays and their implications for GPS/GLONASS PPP-based zenith tropospheric delay and height estimations," *J. Geodesy*, vol. 95, no. 7, p. 83, Jul. 2021, doi: 10.1007/s00190-021-01535-3.

[51] P. Sun, K. Zhang, S. Wu, M. Wan, and Y. Lin, "Retrieving precipitable water vapor from real-time precise point positioning using VMF1/VMF$_3$ forecasting products," *Remote Sens.*, vol. 13, no. 16, p. 3245, Aug. 2021, doi: 10.3390/rs13163245.

[52] F. Li, J. Li, L. Liu, L. Huang, L. Zhou, and H. He, "Machine learning-based calibrated model for forecast Vienna mapping function 3 zenith wet delay," *Remote Sens.*, vol. 15, no. 19, p. 4824, Oct. 2023, doi: 10.3390/rs15194824.

[53] X. Ma, Y. Yao, B. Zhang, and C. He, "Retrieval of high spatial resolution precipitable water vapor maps using heterogeneous Earth observation data," *Remote Sens. Environ.*, vol. 278, Sep. 2022, Art. no. 113100, doi: 10.1016/j.rse.2022.113100.

[54] X. Wang et al., "The correlation between GNSS-derived precipitable water vapor and sea surface temperature and its responses to el Niño–Southern oscillation," *Remote Sens. Environ.*, vol. 216, pp. 1–12, Oct. 2018, doi: 10.1016/j.rse.2018.06.029.

[55] J. Ding and J. Chen, "Assessment of empirical troposphere model GPT3 based on NGL's global troposphere products," *Sensors*, vol. 20, no. 13, p. 3631, Jun. 2020, doi: 10.3390/s20133631.

[56] P. Mateus, J. Catalão, V. B. Mendes, and G. Nico, "An ERA5-based hourly global pressure and temperature (HGPT) model," *Remote Sens.*, vol. 12, no. 7, p. 1098, Mar. 2020, doi: 10.3390/rs12071098.

[57] P. Mateus, V. B. Mendes, and S. M. Plecha, "HGPT2: An ERA5-based global model to estimate relative humidity," *Remote Sens.*, vol. 13, no. 11, p. 2179, Jun. 2021, doi: 10.3390/rs13112179.

[58] L. Huang, G. Zhu, H. Peng, L. Liu, C. Ren, and W. Jiang, "An improved global grid model for calibrating zenith tropospheric delay for GNSS applications," *GPS Solutions*, vol. 27, no. 1, p. 17, Jan. 2023, doi: 10.1007/s10291-022-01354-9.

[59] T. Li et al., "Refining the empirical global pressure and temperature model with the ERA5 reanalysis and radiosonde data," *J. Geodesy*, vol. 95, no. 3, p. 31, Mar. 2021, doi: 10.1007/s00190-021-01478-9.

[60] G. Blewitt, W. Hammond, and C. Kreemer, "Harnessing the GPS data explosion for interdisciplinary science," *Eos*, vol. 99, Sep. 2018, doi: 10.1029/2018eo104623.

[61] I. Durre, X. Yin, R. S. Vose, S. Applequist, and J. Arnfield, "Enhancing the data coverage in the integrated global radiosonde archive," *J. Atmos. Ocean. Technol.*, vol. 35, no. 9, pp. 1753–1770, Sep. 2018, doi: 10.1175/JTECH-D-17-0223.1.

[62] J. Ding, J. Chen, J. Wang, and Y. Zhang, "Characteristic differences in tropospheric delay between Nevada geodetic laboratory products and NWM ray-tracing," *GPS Solutions*, vol. 27, no. 1, p. 47, Jan. 2023, doi: 10.1007/s10291-022-01385-2.
[63] B. Hardy, "ITS-90 formulations for vapor pressure, frostpoint temperature, dewpoint temperature, and enhancement factors in the range -100to +100 C," in *Proc. 3rd Int. Symp. Humid. Moist.*, London, U.K., 1998, pp. 1–8.
[64] A. Wexler, "Vapor pressure formulation for water in range 0 to 100 C. A revision," *J. Res. Nat. Bur. Standards Sect. A, Phys. Chem.*, vol. 80A, nos. 5–6, p. 775, Sep. 1976, doi: 10.6028/jres.080a.071.
[65] A. Wexler, "Vapor pressure formulation for ice," *J. Res. Nat. Bur. Standards A, Phys. Chem.*, vol. 8lA, no. 1, p. 5, Jan. 1977, doi: 10.6028/jres.081A.003.
[66] R. Bommasani et al., "On the opportunities and risks of foundation models," 2021, *arXiv:2108.07258*.
[67] H. Kraus, *Die Atmosphäre der Erde: Eine Einführung die Meteorologie*. Berlin, Germany: Springer, 2001.
[68] J. Ding, J. Chen, J. Wang, and Y. Zhang, "A novel method for tropospheric delay mapping function vertical modeling," *J. Geodesy*, vol. 98, May 2024, Art. no. 37, doi: 10.1007/s00190-024-01845-2.
[69] C. Rocken, S. Sokolovskiy, J. M. Johnson, and D. Hunt, "Improved mapping of tropospheric delays," *Atmos. Ocean. Technol.*, vol. 18, no. 7, pp. 1205–1213, Jul. 2001.
[70] V. Nafisi, M. Madzak, J. Böhm, A. A. Ardalan, and H. Schuh, "Ray-traced tropospheric delays in VLBI analysis," *Radio Sci.*, vol. 47, no. 2, pp. 1–17, Apr. 2012, doi: 10.1029/2011RS004918.
[71] *U.S. Standard Atmosphere*, COESA, United States, National Oceanic and Atmospheric Administration, Washington, DC, USA, 1976 vol. 76, no. 1562.
[72] J. M. Wallace and P. V. Hobbs, "Atmospheric thermodynamics," in *Atmospheric Science*. Amsterdam, The Netherlands: Elsevier, 2006, pp. 63–111, doi: 10.1016/B978-0-12-732951-2.50008-9.
[73] F. Kleijer, *Troposphere Modeling and Filtering for Precise GPS Leveling*. Delft, The Netherlands: Netherlands Geodetic Commission, 2004.
[74] T. Hobiger, S. Shimada, S. Shimizu, R. Ichikawa, Y. Koyama, and T. Kondo, "Improving GPS positioning estimates during extreme weather situations by the help of fine-mesh numerical weather models," *J. Atmos. Solar-Terr. Phys.*, vol. 72, nos. 2–3, pp. 262–270, Feb. 2010, doi: 10.1016/j.jastp.2009.11.018.
[75] J. Böhm, D. Salstein, M. M. Alizadeh, and D. D. Wijaya, "Geodetic and atmospheric background," in *Atmospheric Effects in Space Geodesy*, J. Böhm and H. Schuh, Eds., Berlin, Germany: Springer, 2013, pp. 1–33, doi: 10.1007/978-3-642-36932-2_1.
[76] A. Hofmeister, "Determination of path delays in the atmosphere for geodetic VLBl by means of raytracing," Ph.D. dissertation, Dept. Geodesy Geoinf., Vienna Univ. Technol., Vienna, Austria, 2016.
[77] E. Smith and S. Weintraub, "The constants in the equation for atmospheric refractive index at radio frequencies," *Proc. IRE*, vol. 41, no. 8, pp. 1035–1037, Aug. 1953, doi: 10.1109/JRPROC.1953.274297.
[78] J. M. Rueger, "Refractive index formulae for radio waves," in *Proc. 22nd Int. CongrIntegr, Techn. Corrections Achieve Accurate Eng.*, Washington, DC, USA, 2002, p. 13.
[79] J. M. Rüeger, "Refractive indices of light, infrared and radio waves in the atmosphere," School Surveying Spatial Inf. Syst., Univ. New South Wales, Sydney, NSW, Australia, Tech. Rep. UNISURV S-68, 2002.
[80] G. Chen and T. A. Herring, "Effects of atmospheric azimuthal asymmetry on the analysis of space geodetic data," *J. Geophys. Res., Solid Earth*, vol. 102, no. B9, pp. 20489–20502, Sep. 1997.

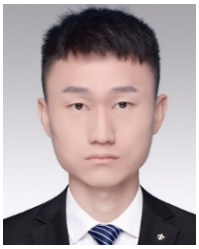

Junsheng Ding received the bachelor's degree from Chang'an University, Xi'an, China, in 2018, and the joint Ph.D. degree from Shanghai Astronomical Observatory, Chinese Academy of Sciences, Beijing, China, and the School of Astronomy and Space Science, University of Chinese Academy of Sciences, Beijing, in 2023.

He is currently a Post-Doctoral Fellow with the Department of Land Surveying and Geo-Informatics, The Hong Kong Polytechnic University (PolyU), Hong Kong. His research interests include Global Navigation Satellite System (GNSS) meteorology and artificial intelligence (AI) for geodesy.

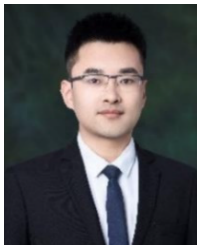

Xiaolong Mi received the Ph.D. degree from the University of Chinese Academy of Sciences, Beijing, China, in 2022, and the Ph.D. degree from Curtin University, Perth, WA, Australia, in 2023.

He is currently a Research Assistant Professor with the Department of Land Surveying and Geo-Informatics, The Hong Kong Polytechnic University, Hong Kong. His research interests include Global Navigation Satellite System (GNSS) and low Earth orbit (LEO) technologies for positioning, navigation, and timing (PNT) along with the application of artificial intelligence (AI) in Earth and space sciences.

Wu Chen received the Ph.D. degree from Newcastle University, Newcastle upon Tyne, U.K., in 1992.

He is currently a Professor with the Department of Land Surveying and Geo-Informatics, The Hong Kong Polytechnic University, Hong Kong. He has been actively working on Global Navigation Satellite System (GNSS)-related research for more than 30 years. His main research interests include GNSS positioning quality evaluation, system integrity, various GNSS applications, seamless positioning, and simultaneous localization and mapping (SLAM).

Junping Chen (Member, IEEE) received the Ph.D. degree in satellite geodesy from Tongji University, Shanghai, China, in 2007.

He is a Professor and the Head of the GNSS Data Analysis Group, Shanghai Astronomical Observatory (SHAO), Chinese Academy of Sciences, Shanghai. Since 2011, he has been supported by the "one hundred talents" programs of Chinese Academy of Sciences. His research interests include multi-Global Navigation Satellite System (GNSS) data analysis and GNSS augmentation systems.

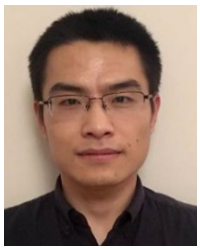

Jungang Wang received the Ph.D. degree from the Technische Universität Berlin, Berlin, Germany, in 2021.

He is a Research Scientist at the Section of Space Geodetic Techniques, GeoForschungsZentrum (GFZ), Potsdam, Germany. His research interests are atmospheric effects in space geodesy, Global Navigation Satellite Systems, very long baseline interferometry, satellite laser ranging, and multitechnique integrated processing.

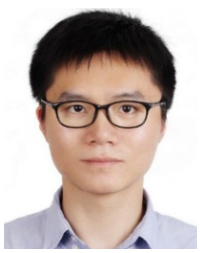

Yize Zhang received the Ph.D. degree from Tongji University, Shanghai, China, in 2017.

After his Ph.D. degree, he did his post-doctoral research at Tokyo University of Marine Science and Technology (TUMSAT), Tokyo, Japan. He is currently an Associate Professor at Shanghai Astronomical Observatory (SHAO), Chinese Academy of Sciences, Shanghai. His research mainly focuses on multi-Global Navigation Satellite System (GNSS) precise positioning and GNSS bias analysis.

Joseph L. Awange received the Ph.D. degree in geodesy from Stuttgart University, Stuttgart, Germany, in 2002.

He is currently engaged in teaching and research with the Spatial Sciences Discipline, School of Earth and Planetary Sciences (EPS), Curtin University, Perth, WA, Australia. He was awarded a merit scholarship by German Academic Exchange Program (DAAD), for his second M.Sc. and Ph.D. degrees.

Benedikt Soja (Member, IEEE) received the Ph.D. degree in geodesy and geoinformation from the Technische Universität Wien, Vienna, Austria, in 2016.

He is currently an Assistant Professor of Space Geodesy with ETH Zürich, Zürich, Switzerland. He became a fellow of the NASA Postdoctoral Program at the Jet Propulsion Laboratory, Pasadena, CA, USA. His research interests include the determination of atmospheric parameters with space-geodetic techniques and the application of machine learning in geodesy.

Lei Bai was a Post-Doctoral Research Fellow at The University of Sydney, Sydney, NSW, Australia. He is currently a Research Scientist with Shanghai AI Laboratory, Shanghai, China. He is leading the OpenEarthLab. His research interests include machine learning, spatial–temporal learning, and their applications.

Dr. Bai was a recipient of the 2020 Google Ph.D. Fellowship, the 2020 UNSW Engineering Excellence Award, and the 2021 Dean's Award for Outstanding Ph.D. Theses.

Yuanfan Deng received the B.S. and M.S. degrees from the School of Geodesy and Geomatics, Wuhan University, Wuhan, China, in 2019 and 2022, respectively. He is currently pursuing the Ph.D. degree with the Department of Land Surveying and Geoinformatics, The Hong Kong Polytechnic University, Hong Kong.

His research focuses on precise Global Navigation Satellite System (GNSS) positioning.

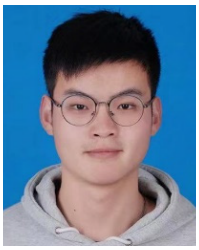

Wenjie Tang received the bachelor's degree from Shanghai Ocean University, Shanghai, China, in 2019. He is currently pursuing the Ph.D. degree with Shanghai Astronomical Observatory (SHAO), Chinese Academy of Sciences (CAS), Shanghai.

His ongoing research focuses on pseudolite precise positioning and atmospheric model correction.